Study on spin-charge conversion in Bi-based systems

Masayuki Matsushima

2022

Study on spin-charge conversion in Bi-based systems

Graduate School of Engineering

Kyoto University

Masayuki Matsushima

2022

Chapter 1. Introduction

1.1 Spintronics and spin current

Spintronics is one of the regions in physics where both charge and spin of electrons are employed for studying condensed matter physics and developing nanoscale devices as memories. As a result of observations and experiments about electricity, magnetism, and quantum mechanism in a long history, spintronics has begun since 1988, when A. Fert from France and P. Grünberg from Germany independently discovered the giant magneto resistivity (GMR) [1,2]. The phenomenon emerges in a sample with trilayer structure, where a nonmagnetic layer is sandwiched between ferromagnetic layers. In this trilayer, directions of magnetizations of each ferromagnetic later are antiparallel under no application of magnetic field, and, on the other hand, directions of the magnetizations are parallel under the application of magnetic field. Here, perpendicular electric current is applied to the trilayer. Electrons with the spin parallel to the magnetization scatter at low probability, where as those with the spin antiparallel to the magnetization scatter at high probability. When electric current passes through the trilayer with antiparallel magnetizations, both states of spin are strongly scattered in each ferromagnetic layer, resulting in high resistance. On the other hand, when the trilayer has parallel magnetizations, only either state of spin is strongly scattered in both ferromagnetic layers, resulting in low resistance. The change in the resistance of trilayer, that is the GMR, is several percent higher than that emerging in a single ferromagnetic layer. The phenomenon has been applied to a head of hard disc drive and has supported information technology society. The discovery of GMR and the introduction of spin current explained in the following are breakthroughs and have expanded the horizon of spintronics.

In general, an electric current is composed of the equal amount of each state of spin. In a ferromagnetic material, the total amount of each spin is biased and electric current is polarized. The spin-polarized electric current performs as a carrier of not only charge but also spin, which indicates that it enables one to flip magnetization without magnetic field [3-5]. The fact that magnetization can be operated without a coil enhances the importance of spin-polarized electric current. However, generation of the polarized current possible to flip magnetizations requires high electric current density, which cannot be easily generated. Here, the concept of pure spin current is introduced, which is a flow of only spin, whereas spin-polarized electric current is a flow of both charge and spin. Both spin-polarized electric current and pure spin current are kinds of spin current. The pure spin current ideally generates no excessive heat, unlike the spin-polarized electric current, and, however, requires the conversion into observables when it is detected.

When electrons scatter in a bulk, the direction of scattering is dependent on their state

of spin. The anisotropic scattering is induced by a coupling between the spin angular momentum of electron and the orbit angular momentum of atoms consisting the bulk, that is, the spin-orbit coupling (SOC). This physics enables one to convert a longitudinal charge current into a transverse spin current in a bulk [6-8], especially in a sheet, and vice versa [9-11]. In addition to the spin-charge conversion in a bulk, it can be realized in other systems. In a system with broken spatial inversion symmetry, such as interfaces between two materials or surfaces, an electric field perpendicular to the planes emerges. The electric field causes a spin splitting in dispersion curve. The change in the band structure of interfaces or surfaces is named the Rashba effect [12]. In a system exhibiting the effect, the movement of electrons is limited to one direction, which depends on the state of spin and the direction of spin polarization. As a result of this limitation, a charge current in a plane is converted into a spin current perpendicular to the plane [13], and vice versa [14]. The discovery of the interconversion phenomena between charge and spin in a simple system has promoted the employment of spin current and has accelerated spin-related physics. Today, several phenomena enable one to convert spin current into electric current, heat, light, vibration, and other physical quantities, and conversely to convert them into spin current [15].

However, the state of spin in a spin current can flip due to the SOC [16-18], and the spin current disappears in a few tens of nanometers or at most one micrometer. A high SOC interferes with the long transportation of spin current. On the other hand, the spin-dependent anisotropic scattering in bulks results in the spin-charge interconversion. High conversion efficiencies was reported for materials with high SOCs [19,20]. For wide variety of materials, the transportable length of spin current and the spin-charge conversion efficiency by the effects in bulks are trade-offs. In addition, the magnitude and polarity of the SOC are related to electron orbitals in atoms, and are dependent on the kind of materials. Therefore, numerous materials have been studied for both spin transportation and spin conversion, depending on the intensity of SOC.

1.2 Bi in spintronics

Bismuth (Bi) is one of the most remarkable elements in solid state physics, since several physical phenomena such as the diamagnetism, the Nernst effect, and the de Haas-van Alphen effect, have been discovered through Bi. The peculiar electron structure of Bi like Dirac electron causes several discoveries of physical phenomena. In spintronics, the SOC is one of the notable properties of Bi. Roughly speaking, the heavier an atom is, the higher the magnitude of the SOC is. In particular, according to a model of the Hydrogen atom, the magnitude of the SOC is proportional to the fourth power of atomic number Z. Figure 1-1 shows the calculated SOC as a function of Z [21]. Although the SOCs are not at all proportional to the fourth power of Z, they

overall tend to increase as an atomic number increases. This figure shows that Bi, one of the heavy elements, exhibits the highest SOC among non-radioactive elements [21,22], which can be easily used for study and application. The current understanding of the spin-charge conversion is that the magnitude of the SOC mainly rules the conversion efficiency [19]. Therefore, the great

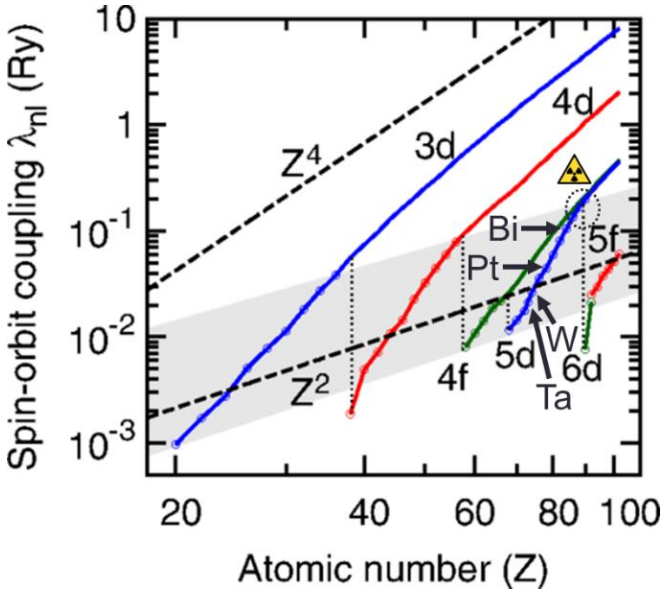

Figure 1-1. Magnitude of spin-obit coupling as a function of atomic number. **Figure adapted from**: K. V. Shanavas *et al*., Phys. Rev. B **90**, 165108 (2014) [21]. Note that the author has made some additions to the original figure.

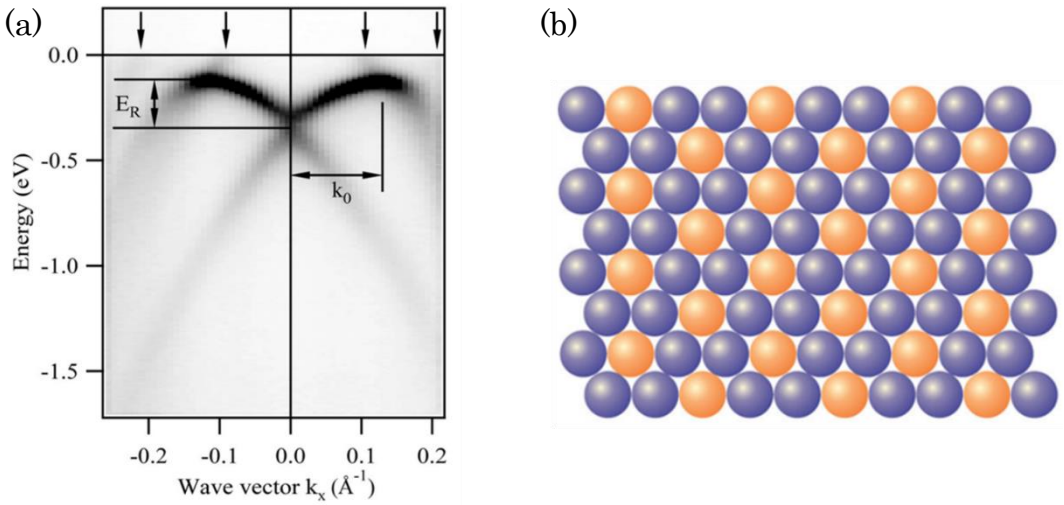

Figure 1-2. (a) Experimentally observed band structure obtained by the angle-resolved photoelectron spectroscopy, and (b) Bi/Ag(111) surface alloy with long-range ordered $(\sqrt{3} \times \sqrt{3})R30°$ Bi (orange) atoms and Ag (blue) atoms. **Figures adapted from**: C. R. Ast *et al*., Phys. Rev. Lett. **98**, 186807 (2007) [23].

magnitude of the SOC of Bi has increased its importance in spintronics.

Moreover, Bi has also played a pivotal role on spin-charge conversion in an interface and a surface. The emergence of the Rashba effect has been predicted and observed in Bi-based systems. Especially, a giant splitting in dispersion curve due to the Rashba effect as shown in Fig. 1-2 (a) has been directly observed at the surface alloy Bi/Ag(111), where the 1/3 of Ag(111) is periodically replaced by Bi (see Fig. 1-2 (b)) [23]. In addition, the giant electric current converted at the Bi/Ag interface was detected [24]. The employment of Bi as one layer of interfaces has enhanced the importance of Bi even more. The property of high SOC brings about a wide employment of Bi in spintronics as a simple substance [25-27], an interface between Bi and another material [24,28], compounds like topological insulators [29-34], and dopants for other materials [35,36].

However, several problems lie in the spin-charge conversion in Bi-based systems. In spite of high SOC, the reported spin-charge conversion efficiencies of Bi were not so high, compared with β-Ta [37], β-W [38], Pt [39,40], and other materials [19,20], which shows less SOC than that of Bi (see Fig. 1-1). Even some studies demonstrated negligible spin-related signals in Bi [41,42]. Although only the magnitude of SOC in atoms is not directly related to highly efficient conversion, the cause of less efficiency of Bi has not been identified yet. For the Rashba effect, many researchers still have discussed the spin-charge conversion at the Bi/Ag interface, since it has not determined whether only the Bi/Ag interface contributes to the spin-charge conversion, or whether the system with the Bi/Ag as a whole system contributes to the spin-charge conversion [41,42]. Many open question remain in spintronics with Bi-based systems.

1.3 Outline of the dissertation

The author reports the results of the studies on spin-charge conversion in Bi-based systems, especially Bi/Ag interface, and Bi film. In Chapter 2, the author introduces physics related to this dissertation, such as spin-charge conversion effects, magnetization dynamics, and spin injection methods. In Chapter 3, the spin-charge conversion in Bi/Ag system is discussed by changing several condition from the previous study. In Chapter 4, the spin-charge conversion in Bi/Py system is investigated. In Chapter 5, the spin-charge conversion in highly oriented Bi grown on single-crystalline Fe is studied by the same method as the previous chapter. Finally, in Chapter 6, the author summarizes the results in this dissertation.

Chapter 2. Physics in spintronics

2.1 Spin-charge conversion

One cannot detect any spin current without the conversion into such observables. The interconversion between spin current and charge current, heat, light, and vibration has been discovered [15]. Here, the author introduces phenomena to convert a charge current into a spin current, and, in reverse, to convert a spin current into a charge current in a bulk or a plane.

2.1.1 Spin Hall effect and inverse spin Hall effect

The SOC is an interaction between spin angular momentum and orbit angular momentum of electrons. When electrons, moving in the same direction with the same momenta, are scattered by a scattering centre in a material, the scattering direction slightly changes depending on their state of spins, due to the SOC. This anisotropic scattering of electrons causes the conversion of a longitudinal charge current into a transverse spin current and vice versa in a macroscopic view. Figure 2-1 (a) shows hehaviour of electrons that form charge current in a material. When a longitudinal charge current is applied, the electrons are scattered in the directions depending on the states of spin. In Fig. 2-1 (a), an electron with spin-up scatters in the left direction, whereas that with spin-down in the right direction. This anisotropic scattering causes finally results in a pure spin current. This phenomenon of converting a longitudinal charge current into a transverse spin current is named the spin Hall effect (SHE) [6-8]. The SHE is one of the fundamental methods to generate a spin current.

A spin current can be also converted into a charge current due to the same physics. Figure 2-1 (b) shows behaviour of electrons that form spin current in a material. In this figure, an electron with spin-up scatters in the left. On the other hand, that with spin-down scatters in the right. The electrons with both states of spin scatter at the same direction, causing a charge current.

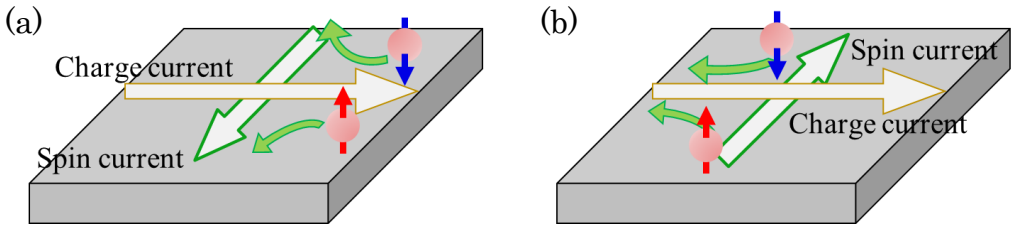

Figure 2-1. Schematic illustrations of (a) the spin Hall effect (charge to spin conversion), and (b) the inverse spin Hall effect (spin to charge conversion)

The phenomenon of converting a longitudinal spin current into a transverse charge current is called the inverse spin Hall effect (ISHE) [9-11].

A spin-charge conversion efficiency of the SHE and the ISHE is featured by a spin Hall angle. In the case of the ISHE, the spin Hall angle is given by the following equation:

$$\boldsymbol{j_c} = \boldsymbol{\theta_{SHE}}\left(\frac{\boldsymbol{2e}}{\hbar}\right)\boldsymbol{j_s} \times \hat{\boldsymbol{\sigma}}, \tag{2.1}$$

where $\boldsymbol{j_c}$ is a transverse charge current, $\boldsymbol{j_s}$ a longitudinal spin current, $\hat{\boldsymbol{\sigma}}$ a spin polarization of electrons in the spin current, e the elementary charge, $\hbar$ the reduced Planck constant, and θ_{SHE} the spin Hall angle, respectively. Here, the coefficient of $2e/\hbar$ changes the dimension of spin current into that of charge current, by dividing by electron spin $\hbar/2$ and multiplying by electron charge e. In the case of the SHE, the spin Hall angle can be given by the equation, where the positions of $\boldsymbol{j_c}$ and $\boldsymbol{j_s}$ are replaced, and the spin Hall angles of the SHE and the ISHE are equivalent.

The magnitude and polarity of spin Hall angles depend on the kind of materials, whose SOCs vary in the magnitude and polarity [19,20]. As mentioned in Chapter 1, the magnitude of the SOC is proportional to the fourth power of atomic number in a simplified model. Figure 2-2 shows the magnitude of spin Hall angle as a function of the fourth power of atomic number Z [19]. The spin Hall angles are proportional to Z^4 except W. This fact provides a basis for the expectation of a large spin Hall angle for materials with a high SOC.

Finally, the spin diffusion length is explained, which is one of the important quantities for spin conversion physics. In the process of the spin-charge conversion, a spin current advancing

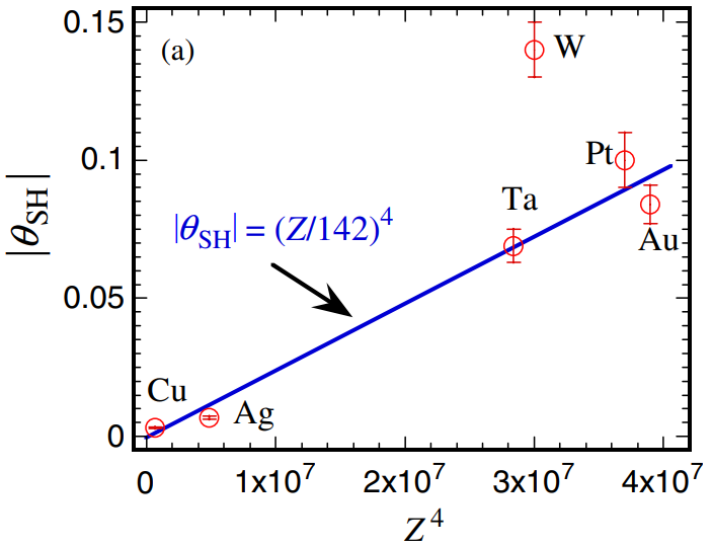

Figure 2-2. Magnitude of spin Hall angle as a function of the fourth power of atomic number Z, with a line proportional to Z^4. **Figure adapted from**: H. L. Wang *et al.*, Phys. Rev. Lett. **112**, 197201 (2014) [19].

through a material dissipates, and a part of dissipated spin current is converted into a charge current. The distance of dissipation of the spin current into $1/e$ is described by the spin diffusion length. The size of the spin diffusion length also depends on the kind of materials. A spin Hall angle and a spin diffusion length are the tradeoff relation in general.

2.1.2 Rashba-Edelstein effect and inverse Rashba-Edelstein effect

Rashba has demonstrated that a split of band structure in k-space shown in Fig. 2-3 (a) emerges in a system with breaking spatial symmetry like an interface or a surface [12]. In the system with the asymmetry, an electric field perpendicular to the plane occurs. The electric field is regarded as an effective magnetic field in the region of the special relativity. A kind of SOCs, that is, a coupling of the magnetic field and electron spin causes the split of dispersion curve shown in Fig. 2-3 (a). On the Fermi surface, the split band forms two concentric circles with different radii like Fig. 2-3 (b). Each circle is composed of electrons with each state of spin, respectively. In this system, the direction of motion of electrons is determined by the state of spin and the direction of spin polarization.

When an in-plane charge current is injected to the system in the $+x$ direction, an electric field is applied in the $-x$ direction, and the field moves both concentric circles in $+x$ direction for the same distance shown in Fig. 2-3 (c). The red region is the difference before and after the movement of the large red circle. Since the electron at the right side of the red circle exhibits spin polarization in the $+y$ direction, the difference causes spin polarization in the direction. On the other hand, the blue region is the difference before and after the movement of the small blue circle. Since the electron at the right side of the blue circle exhibits spin polarization in the $-y$ direction, the difference causes spin polarization in the direction, which is opposite to the direction of spin polarization by the red circle. A part of the red region remains as the difference in the area between the red and blue regions, and spins polarized in the $+y$ direction are accumulated. The generation of spin accumulation due to the difference in the radius of two circles with different types of spin is called the Edelstein effect, or the Rashba-Edelstein effect (REE) [13]. The spin accumulation causes a spin current perpendicular to the interface or surface. Hence, the REE can be regarded as a phenomenon of charge-to-spin conversion.

When an out-of-plane spin current with spin polarization in the $+y$ direction is injected to the interface or surface, the polarized spin is accumulated and each concentric circle shifts according to the polarized direction. In Fig. 2-3 (d), the large red circle moves in the $+x$ direction, and the small blue circle in the $-x$ direction. The area of red region causes a flow of electron in the $+x$ direction, and the area of blue region causes a flow of electron in the $-x$ direction,

respectively. Since the red area is larger than the blue area, the net flow of electron exists in the $+x$ direction. That is the existence of the charge current in the $-x$ direction. This phenomenon of the conversion of out-of-plane spin current into in-plane charge current is the inverse Edelstein effect or the inverse Rashba-Edelstein effect (IREE) [14,24]. The spin-to-charge conversion efficiency by the IREE is given by

$$j_c^{2D} = \left(\frac{2e}{\hbar}\right)\lambda_{IREE} j_s, \tag{2.2}$$

where j_c^{2D} is two-dimensional charge current density in the plane, j_s spin current density normal to the plane, and λ_{IREE} the Rashba length, i.e., the spin-to-charge conversion efficiency, respectively. This phenomenon converts three-dimensional out-of-plane spin current into two-

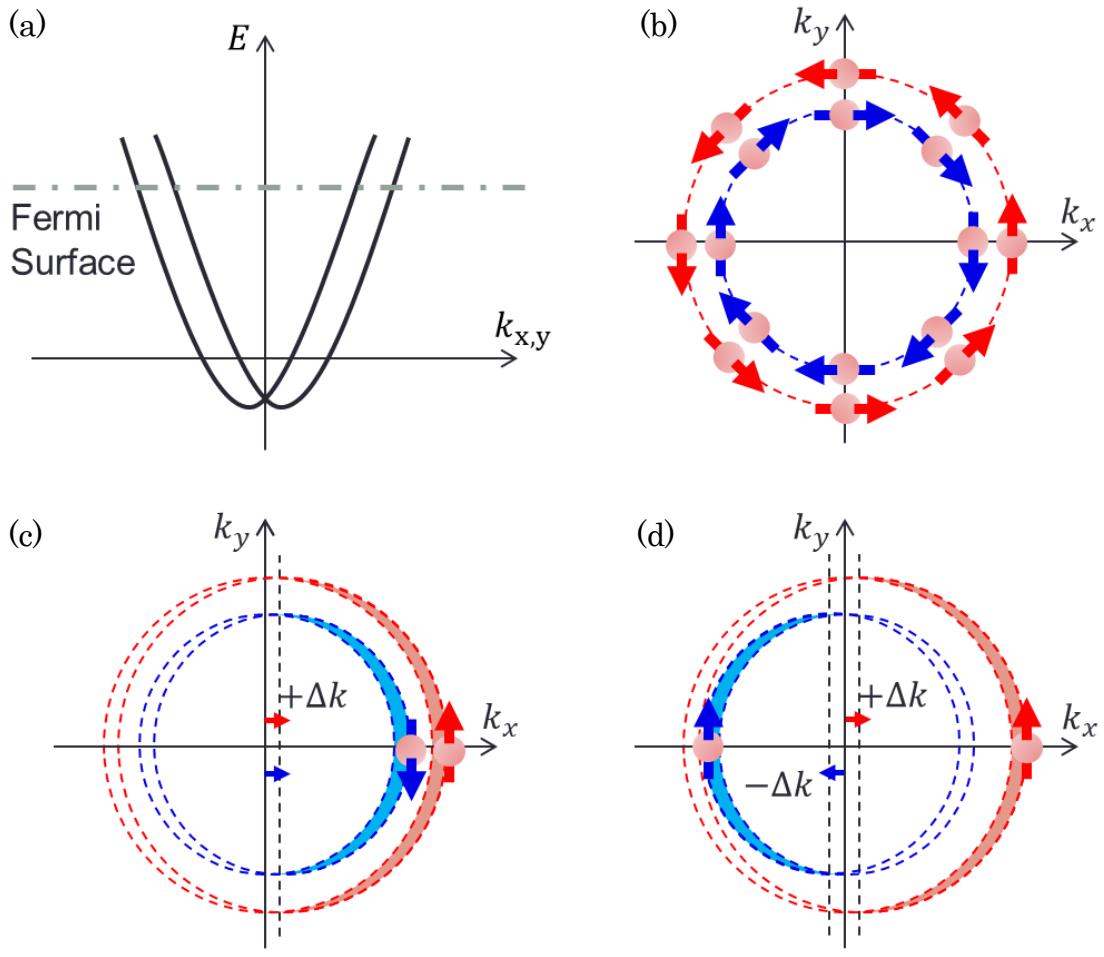

Figure 2-3. (a) Dispersion curve induced by the Rashba effect, (b) concentric circles on the Fermi surface with different radii, the size of which is dependent on the state of spin, (c) the circles moving in the same direction, causing in the Rashba-Edelstein effect (charge to spin conversion), and (d) the circles moving in the opposite directions, causing in the inverse Rashba-Edelstein effect (spin to charge conversion)

dimensional in-plane charge current. Hence, the Rashba length has the dimension of length.

2.2 Spin relaxation mechanism

While spin current flows, a part of the spins changes their state and phase due to the SOC. Here, two kinds of spin relaxation mechanism, the Elliott-Yafet (EY) mechanism (see Fig. 2-4 (a)) [16,17], and the D'yakonov-Perel' (DP) mechanism (see Fig. 2-4 (b)) [18], are introduced.

2.2.1 Elliott-Yafet mechanism

When electrons are scattered by scattering centres like impurities, in addition to a change in the direction of motion, the state of their electron spins can also flip with a certain probability due to the SOC. The correlation between momentum relaxation and spin relaxation of electrons are given by

$$\frac{1}{\tau_s} \propto \frac{1}{\tau_p}, \tag{2.3}$$

where τ_s is the spin lifetime, and τ_p the momentum relaxation time, respectively.

2.2.1 D'yakonov-Perel' mechanism

In a system with breaking spatial symmetry, an effective magnetic field induced by the SOC like the Rashba effect is applied to spins. In between two events of electron scatterings, the effective magnetic field forces the spin polarization to make a precession. As each electron is

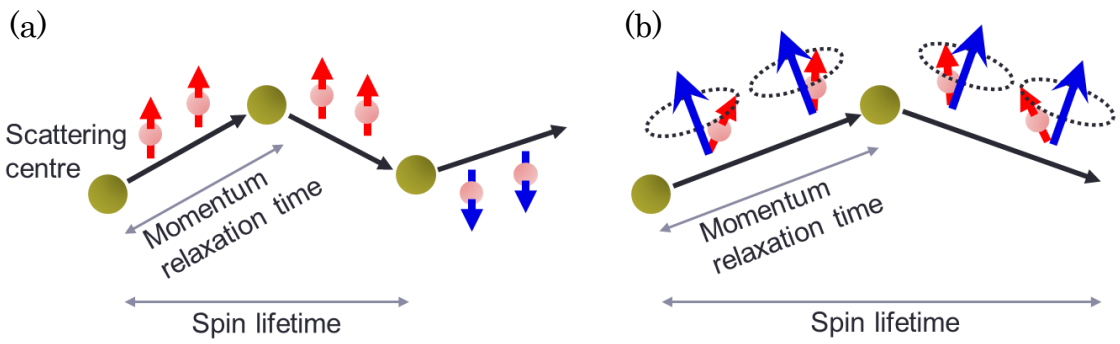

Figure 2-4. Spin relaxation process of (a) the Elliott-Yafet mechanism, and (b) the D'yakonov-Perel' mechanism

scattered by scattering centres, the direction of the applied effective magnetic field and consequently the phase of spin polarization changes for each electron. Finally, the spin current loses the order of spin polarization. In this mechanism, the correlation between momentum and spin relaxation of electrons are given by

$$\frac{1}{\tau_s} \propto \tau_p. \tag{2.4}$$

The correlation between the momentum relaxation time and the spin lifetime is completely different from that of the EY mechanism.

2.2.3 Spin diffusion length and spin lifetime.

Spin relaxation occurs when electrons are scattered by scattering centres or they are applied to effective magnetic field while flowing. Hence, the spin diffusion length and the spin lifetime are closely related. The spin diffusion length λ_s is described as

$$\lambda_s = \sqrt{D\tau_s}, \tag{2.5}$$

where D is the diffusion constant of the electron. By analyzing the constants mentioned here, the spin relaxation mechanism of systems can be estimated.

2.3 Magnetization dynamics

When a ferromagnetic material is applied to both ac magnetic field in microwave and static magnetic field, magnetization in the ferromagnetic material is excited and makes a precession. This resonant phenomenon is named the ferromagnetic resonance (FMR). In the mid-twentieth century, Kittel expanded the relation between the Larmor frequency, the resonant frequency in a sample, and the applied static magnetic field by taking into account the shape anisotropy and the direction of magnetic field [43]. Under the application of magnetic field to a ferromagnetic thin film, which is sufficiently broad in relation to its thickness, the relation between a frequency under the FMR f_0 and the applied magnetic field is described by the Kittel equation as follows:

$$f_0 = \frac{\gamma}{2\pi}\sqrt{\mu_0 H_{\parallel}\mu_0 H_{\perp}}, \tag{2.6}$$

where $\gamma = g\mu_B/\hbar$ is the gyromagnetic ratio, g g-factor of a ferromagnetic material, μ_B the Bohr magneton, and $\mu_0 H_{\parallel}$ and $\mu_0 H_{\perp}$ are in-plane and out-of-plane effective magnetic field under the FMR, respectively. For example, in a sample with no magnetocrystalline anisotropy,

the Kittel equation is described as

$$f_0 = \frac{\gamma}{2\pi}\sqrt{\mu_0 H_{\mathrm{res}}(\mu_0 H_{\mathrm{res}} + \mu_0 M_{\mathrm{eff}})}, \tag{2.7}$$

where $\mu_0 H_{\mathrm{res}}$ is a resonance field, and $\mu_0 M_{\mathrm{eff}}$ is the demagnetization field in the perpendicular direction, respectively. Note that, in a sample with magnetocrystalline anisotropy, some terms are added to $\mu_0 H_{\parallel}$ and $\mu_0 H_{\perp}$ according to materials, crystal orientation, and the direction of applied magnetic field.

According to the theory of magnetization dynamics, the precession of magnetization in ferromagnetic materials is governed by the Landau-Lifshitz-Gilbert (LLG) equation as follows [44,45]:

$$\frac{d\boldsymbol{M}}{dt} = -\gamma \boldsymbol{M} \times \mu_0 \boldsymbol{H}_{\mathbf{eff}} + \frac{\alpha}{M_s}\boldsymbol{M} \times \frac{d\boldsymbol{M}}{dt}, \tag{2.8}$$

where $\boldsymbol{M}$ is the magnetization, $\mu_0 \boldsymbol{H}_{\mathbf{eff}}$ the effective magnetic field, $\mu_0 M_s$ the saturation magnetization, and α the Gilbert damping constant or simply the damping constant, respectively. Figure 2-5 shows a schematic illustration of the precession of magnetization. The magnetization governed by the LLG equation moves on a sphere without changing its magnitude. The first term of the RHS of the LLG equation describes the torque of circumferential direction on a plane perpendicular to the magnetic field, and the second term describes the torque of damping component, which works to point the magnetization in the direction parallel to the magnetic field and to stop the precession, respectively. The calculation of the LLG equation with several approximations enables one to derive the Kittel equation.

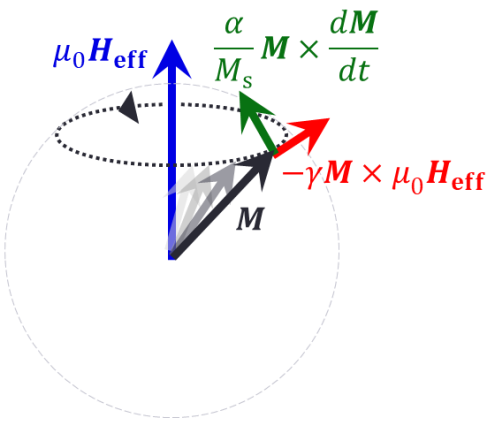

Figure 2-5. Schematic illustration of the precession of magnetization under the application of magnetic field, with vectors introduced by the LLG equation

2.4 Spin pumping and transition of generated spin current

In a bilayer system of metal/ferromagnetic material, electron spins in metallic layer are coupled with the magnetization in the ferromagnetic layer via the exchange interaction. Due to the exchange interaction, an effective magnetic field is applied to electrons in the metallic layer near the interface, and a magnetic moment, that is a magnetization, is generated in the metallic layer. Under the FMR, the magnetization dynamics in the ferromagnetic layer near the interface excites the magnetization in the metallic layer, causing spin accumulation in the metallic layer. In other words, a part of angular momenta in the ferromagnetic layer is transferred to the metallic layer via the exchange coupling. This spin injection method is called the spin pumping method [46,47].

The accumulated spin flows through the metallic layer as a spin current, which dissipates in the layer while flowing, until it reaches the surface of the layer. When the j_{s0} of spin current density is initially injected to the layer, spin current density at z before reaching the surface is described as

$$j_s(z) = e^{-\frac{z}{\lambda_s}} j_{s0}. \tag{2.9}$$

The dissipated spin current is partly converted into charge current due to the ISHE. Hence, when the spin current flows up to z while dissipating, the total amount of generated charge current is given by

$$j_c(z) = \left(\frac{2e}{\hbar}\right)\theta_{SHE}\left(1 - e^{-\frac{z}{\lambda_s}}\right) j_{s0}. \tag{2.10}$$

Note that no spin current reaches the surface of the layer here.

When a spin current reaches the surface of the layer, it is reflected by the surface and flows back. The spin current density concerning the back flow is described as

$$j_s(z) = \frac{\sinh((d-z)/\lambda_s)}{\sinh(d/\lambda_s)} j_{s0}, \tag{2.11}$$

where d is the thickness of the metallic layer. The spin current converts into the charge current in the metallic layer in accordance with Eq. (2.1). Therefore, the average of charge current density in the metallic layer is described as

$$\begin{aligned}\langle \boldsymbol{j_c} \rangle &= \left(\frac{\mathbf{1}}{\boldsymbol{d}}\right)\int_0^{\boldsymbol{d}} \boldsymbol{j_c}(\boldsymbol{z})\boldsymbol{dz} \\ &= \boldsymbol{\theta_{SHE}}\left(\frac{\boldsymbol{2e}}{\hbar}\right)\frac{\boldsymbol{\lambda_s}}{\boldsymbol{d}}\mathbf{tanh}\left(\frac{\boldsymbol{d}}{\boldsymbol{2\lambda_s}}\right)\boldsymbol{j_{s0}},\end{aligned} \tag{2.12}$$

and the charge current I_c is described as $I_c = wd\langle j_c \rangle$, where w is the transverse length of the metallic layer [48].

The spin pumping is a critical method for generating a spin current, since one can apply the method to a bilayer system of metal/ferromagnetic material and estimate the spin Hall angle of the metallic layer by employing Eq. (2.12). By fabricating multiple samples with the metallic layer of different thicknesses and measuring the charge current obtained from each sample, both the spin Hall angle and the spin diffusion length of the metal can be estimated. When one adopts a ferromagnetic metal as a ferromagnetic layer for the spin pumping, a charge current not only by the ISHE in the metallic layer but also by the ISHE in the ferromagnetic metal itself are detected [49,50]. Since the additional signal interferes with the estimation of the spin Hall angle of the metallic material, an insulating magnetic material should be introduced for the magnetic layer.

2.5 Spin torque-ferromagnetic resonance

In addition to the spin pumping method, the spin torque-ferromagnetic resonance (ST-FMR) method also enables one to estimate spin-charge conversion efficiency of a nonmagnetic metal [39,51-53]. Figure 2-6 (a) shows a typical setup of the ST-FMR. When a radio frequency (rf) charge current is conducted to a nonmagnetic metal/ferromagnetic metal bilayer under the application of external magnetic field, magnetization of the ferromagnetic layer makes a precession under the condition of the FMR. The rf charge current through the nonmagnetic layer has an influence on the magnetization by two types of torques: the spin transfer torque (STT) [54], and the field-like torque (FLT) [55]. Figure 2-6 (b) shows a charge current and torques on the magnetization. The charge current converts by the SHE into a spin current, which is injected into the ferromagnetic layer and exerts the STT (light blue arrow) on the magnetization in the direction almost opposite to the torque of the damping term (dark green arrow). On the other hand, the FLT (pink arrow) is exerted by the magnetic field around the rf charge current, in the same direction as the torque of the precession term (red arrow). In this situation, the following equation governs

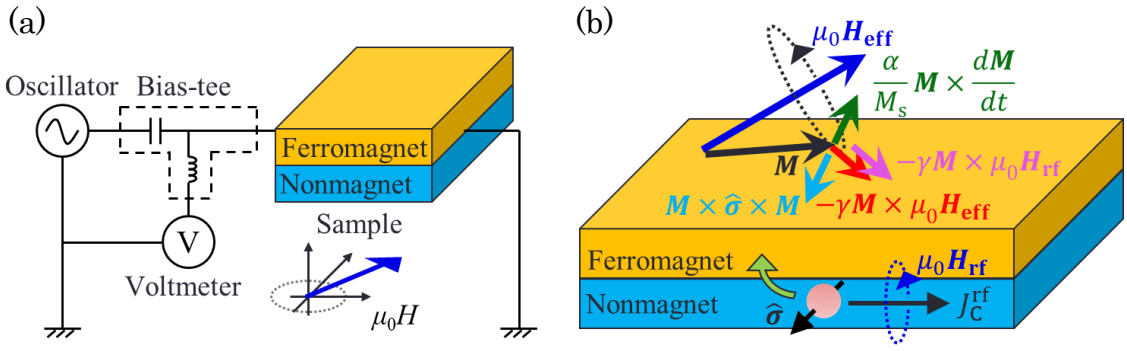

Figure 2-6. (a) Measurement circuit for the spin torque-ferromagnetic resonance method, and (b) vectors concerning the magnetization dynamics

the magnetization dynamics:

$$\frac{d\boldsymbol{M}}{dt} = -\gamma \boldsymbol{M} \times \mu_0 \boldsymbol{H}_{\mathbf{eff}} + \frac{\alpha}{M_\mathrm{s}} \boldsymbol{M} \times \frac{d\boldsymbol{M}}{dt} + \gamma \frac{\hbar J_\mathrm{S}^\mathrm{rf}}{2e\mu_0 M_\mathrm{s}^2 t_\mathrm{F}} (\boldsymbol{M} \times \hat{\boldsymbol{\sigma}} \times \boldsymbol{M}) - \gamma \boldsymbol{M} \times \mu_0 \boldsymbol{H}_{\mathbf{rf}}, \tag{2.13}$$

where $J_\mathrm{S}^\mathrm{rf}(\hbar/2e)$ is an oscillating spin current density, t_F the thickness of the ferromagnetic layer, and $\mu_0 \boldsymbol{H}_{\mathbf{rf}}$ the magnetic field generated by the rf charge current, respectively. The first and the second terms of the RHS are the same as the LLG equation, and the third and the fourth terms describe the STT and the FLT, respectively.

Under the FMR of the ferromagnetic layer, the STT and the FLT induce a time-dependent component in the resistance of the ferromagnetic layer, as a function of the sine with the same frequency as that of the rf charge current. The multiplication of the rf charge current and the time-dependent resistance generates a dc voltage, which can be detected through a bias-tee, by separating the dc voltage from the reflected component of the rf charge current. The dc voltage as a function of an external magnetic field $\mu_0 H$ is given by

$$V = -C\left(S\frac{(\mu_0\Delta H)^2}{(\mu_0\Delta H)^2 + (\mu_0 H - \mu_0 H_\mathrm{res})^2} + A\frac{\mu_0\Delta H(\mu_0 H - \mu_0 H_\mathrm{res})}{(\mu_0\Delta H)^2 + (\mu_0 H - \mu_0 H_\mathrm{res})^2}\right), \tag{2.14}$$

where $\mu_0\Delta H$ is full width at half maximum, C a constant concerning the resistance and the rf charge current and proportional to $\sin\theta\cos^2\theta$ for the θ direction of the in-plane magnetic field, respectively. The first and the second terms in the large bracket are shaped by the symmetric Lorentzian centered at the magnetic resonance field $\mu_0 H_\mathrm{res}$ with full width at half maximum $\mu_0\Delta H$, and the antisymmetric Lorentzian centered at the magnetic resonance field, respectively. Besides, the S and A are given by

$$S = \frac{\hbar J_\mathrm{S}^\mathrm{rf}}{2e\mu_0 M_\mathrm{s} t_\mathrm{F}}, \tag{2.15}$$

$$A = H_\mathrm{rf}\sqrt{\frac{H_\perp}{H_\parallel}}. \tag{2.16}$$

Here, the width of the bilayer is much larger than the thickness of nonmagnetic layer t_N, which results in an approximation; the bilayer can be regarded as infinitely wide plate, and, due to Ampère's law, H_rf is described as $H_\mathrm{rf} = J_\mathrm{C}^\mathrm{rf} t_\mathrm{N}/2$, where J_C^rf is the charge current density in the nonmagnetic layer. Therefore, the charge-to-spin conversion efficiency by the SHE in the ST-FMR method should be given by

$$\eta = \frac{J_\mathrm{S}^\mathrm{rf}}{J_\mathrm{C}^\mathrm{rf}} = \frac{S}{A}\frac{e\mu_0 M_\mathrm{s} t_\mathrm{F} t_\mathrm{N}}{\hbar}\sqrt{\frac{H_\perp}{H_\parallel}}. \tag{2.17}$$

By employing this equation, the spin-charge conversion efficiency as a function of the thickness of nonmagnetic or ferromagnetic layer can be estimated. In particular, according to a sample with no magnetocrystalline anisotropy, this equation can be described as

$$\eta = \frac{S}{A}\frac{e\mu_0 M_s t_F t_N}{\hbar}\sqrt{1+\frac{M_{eff}}{H_{res}}}. \tag{2.18}$$

Note that one does not necessarily regard this conversion efficiency as a quantity equivalent to a spin Hall angle estimated by another method as the spin pumping. The thickness dependence of spin conversion efficiency obtained by the ST-FMR method can be described as

$$\eta = \eta_\infty\left(1-\operatorname{sech}\left(\frac{t_N}{\lambda_s}\right)\right), \tag{2.19}$$

where η_∞ is the saturated value of the spin-charge conversion efficiency [56]. In addition to the change in the spin-charge conversion efficiency, the spin diffusion length of the nonmagnetic layer can be also estimated.

Chapter 3. Inverse Rashba-Edelstein effect in Bi/Ag and Ag/Bi

3.1 Comparison between previous and present study

The previous study in 2013 experimentally demonstrated the existence of the IREE at Bi/Ag interface by introducing Bi/Ag/NiFe system [24]. In the study, the following model of flowing spin current was introduced for analysis. A spin current injected into Ag layer by spin pumping method flew through the layer without dissipation. When it reached Bi/Ag interface, it was completely converted into a charge current. Here, all of the spin current reaching the interface was converted, whereas no spin current was transmitted through the interface nor injected into Bi layer. In addition, no consideration of the dissipation of the spin current in the Ag layer resulted in no consideration of the ISHE in the layer, since a part of dissipated spin current is converted into a charge current. This approximation is based on the long spin diffusion length and small spin Hall angle of Ag [19,57]. Hence, in the previous study, it was considered that the Bi and Ag layers did not contributed to the detected charge current as a single layer and that the origin of the current was entirely the IREE from the Bi/Ag interface.

However, the introduction of NiFe for the spin pumping is a clear problem. The NiFe is a ferromagnetic metal, which generates spurious electromotive forces while the magnetization is excited under the FMR, due to self-induced ISHE [49,50] or other effects [58,59]. The superposition of the electromotive force from the NiFe on the charge current from the Bi/Ag interface interferes with accurate estimation of the IREE.

In this dissertation, the author introduced a ferrimagnetic insulator, yttrium iron garnet (YIG), as a ferromagnetic material for the spin pumping, instead of conductive NiFe. In general, a ferrimagnetic material has two independent magnetic moments with different magnitudes. For YIG, two types of magnetic moments synchronize under the FMR and can be regarded as one magnetic moment, as a vector summation of the two moments. Hence, one employs a ferrimagnetic YIG like a ferromagnetic material. YIG is also an insulator, which generates no unwanted signal induced by the effects explained above. In addition, the author takes into account the dissipation of spin current in Bi and Ag layers, the generation of charge current due to the ISHE, and the transmission through Bi/Ag interface. Furthermore, to study an influence on the polarity of the charge current, the author introduced two types of samples with reversed stacking orders, Bi/Ag/YIG and Ag/Bi/YIG. The Rashba effect is induced by the electric field at the interface. The interface with the reversed stacking orders has the intrinsic electric field in the opposite direction, which generates the charge current with the opposite polarity [60]. Each sample is expected to generate signals with different intensity. By comparing each intensity, a possible range of the spin conversion efficiency by the IREE was estimated.

3.2 Experimental setup

3.2.1 Features of each sample

Bi (7 nm in thickness) and Ag (5 nm) were deposited by using a resistance heating system on 10-μm-thick single-crystalline YIGs, which were grown on gallium gadolinium garnet (GGG) substrates with 5 mm × 2 mm in size. Figures 3-1 (a) and (b) show two types of samples: the Bi/Ag/YIG and the Ag/Bi/YIG. By using the spin pumping method, a pure spin current was injected into the Bi/Ag and Ag/Bi bilayers and converted into charge currents by the ISHE in the Bi and Ag layers and by the IREE at the interface. Here, the stacking order of the Bi and Ag layers rules the direction of intrinsic electric field normal to the interface, which causes the Rashba effect. The direction of the electric field governs the polarity of the charge current at the interface induced by the IREE. Therefore, in the Bi/Ag/YIG system, the charge currents, which were generated in Bi and Ag layers and at the Bi/Ag interface, flew in the same direction, whereas, in the Ag/Bi/YIG system, only the charge current at Ag/Bi interface flew in the opposite direction.

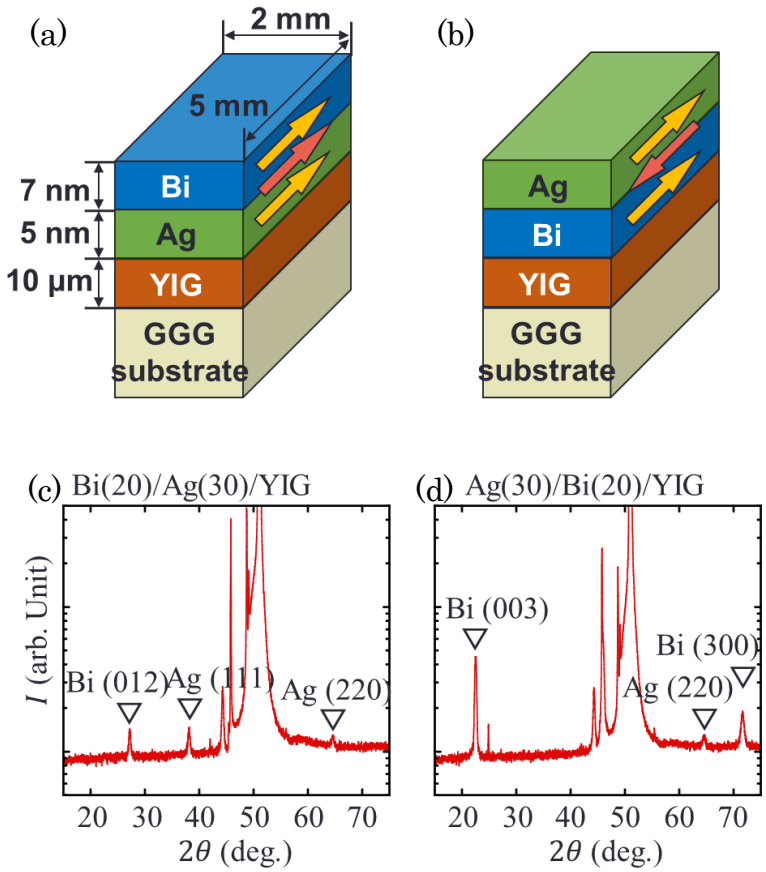

Figure 3-1. (a) Bi/Ag/YIG and (b) Ag/Bi/YIG with charge currents generated by the ISHE (yellow arrow) and by the IREE (red arrow), and XRD spectra obtained from (c) Bi(20 nm)/Ag(30 nm)/YIG and (d) Ag(30 nm)/Bi(20 nm)/YIG

To clarify crystal structure of the Bi and the Ag, the X-ray diffraction was performed on Bi (20 nm)/Ag (30 nm)/YIG and Ag (30 nm)/Bi (20 nm)/YIG. Figures 3-1 (c) and (d) show θ-2θ spectra of each sample, where Cu-Kα radiation was employed. Compared with the previous study [24], where Bi(003) of a rhombohedral structure and Ag(220) were observed with NiFe/Ag/Bi/SiO_2 —Bi, Ag, and NiFe were deposited on SiO_2 substrate in this order—, the similar diffraction pattern was detected from the Ag/Bi/YIG. This result suggests that the crystallographic properties of the Ag/Bi/YIG and the NiFe/Ag/Bi/SiO_2 are similar, and that the existence of the internal electric field induced by the Rashba effect is expected with the similar magnitude. On the other hand, the Bi/Ag/YIG exhibited the peaks of Ag(111) and Bi(012).

3.2.2 Measurement procedure by spin pumping

Figure 3-2 (a) shows a schematic illustration of the sample under measurement. Electrodes were bonded at both ends of the longitudinal direction on the surface, and a nanovoltmeter was connected with them. The sample was inserted into a cavity of an electron spin resonance system (JEOL JES-FA 200) as shown in Fig. 3-2 (b). A microwave with TE_{011} mode was applied to the sample under the application of external magnetic field. The frequency and power of microwave were 9.12 GHz and 1 mW, respectively. Under the FMR of the YIG, a spin current was injected to the Bi/Ag bilayer and converted into a charge current by the ISHE and the IREE, which was measured by a nanovoltmeter. At the same time, the intensity of microwave absorption by the sample was measured with microwave detector in the ESR system.

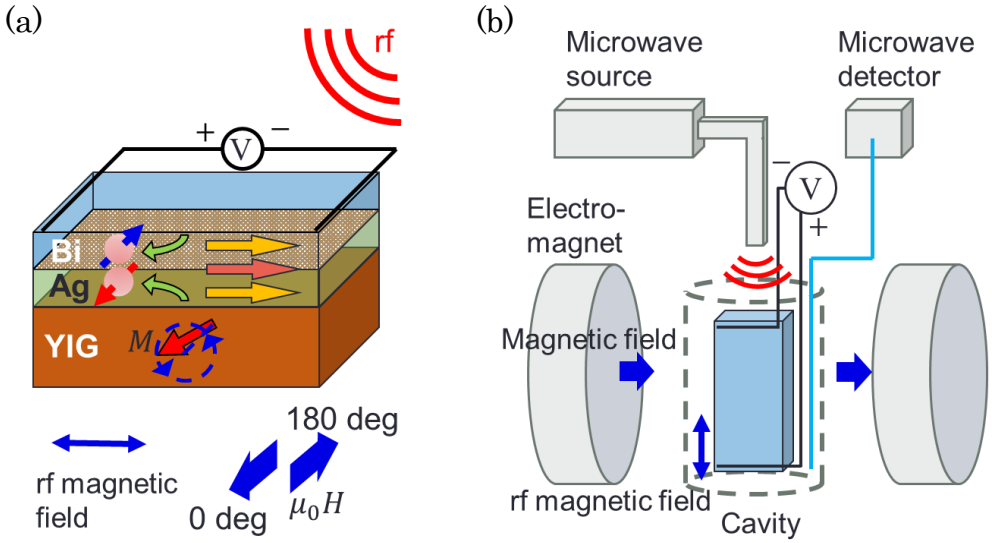

Figure 3-2. Schematic illustrations of (a) Bi/Ag/YIG and (b) Ag/Bi/YIG, and XRD spectra of (c) Bi(20 nm)/Ag(30 nm)/YIG and (d) Ag(30 nm)/Bi(20 nm)/YIG

Here, detected signals include spurious signals by heat-related effects. These spurious components are independent of the direction of the magnetic field. To eliminate the spurious components, the charge currents $I_C(0°)$ and $I_C(180°)$ were measured under the application of magnetic field in the direct direction (0°) and the opposite direction (180°). The charge current induced by both the ISHE and the IREE without heat-related signal was obtained by calculating $I_{C,ave} = \{I_C(0°) - I_C(180°)\}/2$. All measurements were carried out at room temperature.

3.3 Detected currents and spin conversion efficiency

Figures 3-3 (a) and (b) show charge currents generated from the Bi/Ag/YIG and the Ag/Bi/YIG $I_{C,ave}$ as a function of applied magnetic field $\mu_0 H$ minus the resonance field $\mu_0 H_{res}$ (~ 245 mT). Here, the calculation between the signals at the direct (0°) and the opposite (180°) directions was already applied. Figures 3-3 (c) and (d) show spectra of the intensity of microwave absorption I at 0° and 180° obtained from each sample while measuring the charge current signals, respectively. The charge currents were clearly generated at the resonance field of the YIGs, which indicated that the injection of spin currents and the conversion into the charge currents were induced under the FMR. The magnitudes of the charge currents from the Bi/Ag/YIG and the Ag/Bi/YIG were 300 pA and 200 pA, respectively. The polarity of each sample was the same although the internal electric field induced by the Rashba effect exhibited the opposite polarity. It suggests that the consideration of the IREE without the ISHE should not be sufficient.

To interpret the results, the author constructed a model, where the spin-to-charge

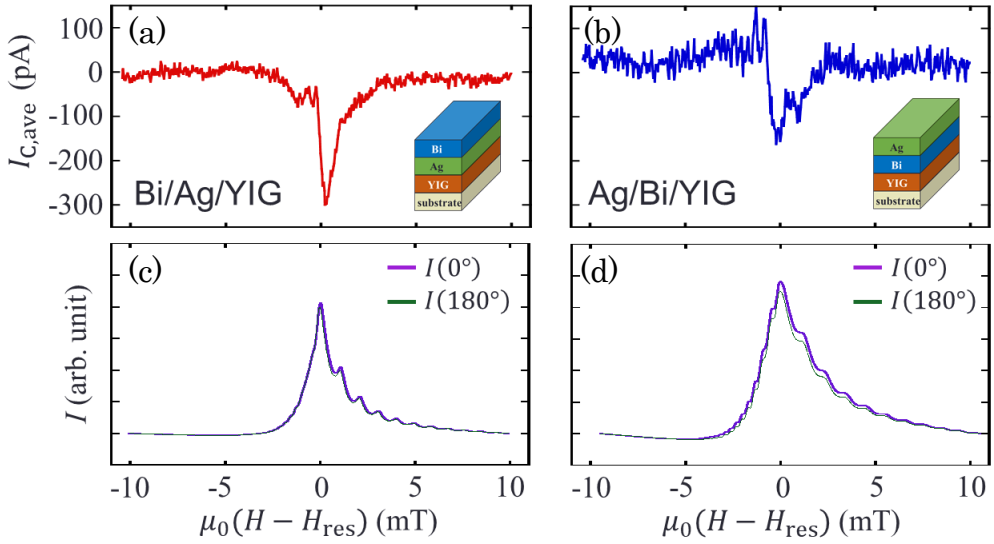

Figure 3-3. Charge currents applied the calculation from (a) Bi/Ag/YIG and (b) Ag/Bi/YIG, and intensity of ESR signals at 0° and 180° obtained from (c) Bi/Ag/YIG and (d) Ag/Bi/YIG

conversion by both the IREE and the ISHE, the dissipation of the spin current in the Bi and Ag layers, and the transmission of the spin current at the Bi/Ag interface were took into account. Here, the author introduced the transmittance of the Bi/Ag interface κ and described the model for the spin current by using the transmittance. Figure 3-4 shows schematic illustrations of models for $\kappa = 0$ and $\kappa = 1$ of each sample, respectively. For $\kappa = 0$, as shown in Figs. 3-4 (a) and (b), the lower limit of transmittance, the injected spin currents advance through the layers adjacent to the YIGs while dissipating and being converted into charge currents by the ISHE, and the spin currents reaching the Bi/Ag interfaces are converted by the IREE and dissipate completely. On the other hand, for $\kappa = 1$, as shown in Figs. 3-4 (c) and (d), the upper limit of transmittance, the spin currents reaching the Bi/Ag interface are transmitted to the other layer completely, while converted by the IREE. The transmitted spin currents are reflected at the surface of the sample and flow back to the YIGs while exhibiting the same behaviour as that in the way to the surface. When $\kappa = [0, 1]$, the generated charge current $I_{\mathrm{C,ave}}$ is given by

$$\begin{aligned} I_{\mathrm{C,ave}} = {} & w\theta_a\lambda_a\left(1 - e^{-\frac{t_a}{\lambda_a}}\right)\left(1 - \kappa^2 e^{-\frac{t_a}{\lambda_a}-\frac{2t_b}{\lambda_b}}\right) j_{\mathrm{s0}}\left(\frac{2e}{\hbar}\right) \\ & \pm w\lambda_{\mathrm{IREE}} e^{-\frac{t_a}{\lambda_a}}\left(1 + \kappa e^{-\frac{2t_b}{\lambda_b}}\right) j_{\mathrm{s0}}\left(\frac{2e}{\hbar}\right) \\ & + \kappa w\theta_b\lambda_b e^{-\frac{t_a}{\lambda_a}}\left(1 - e^{-\frac{t_b}{\lambda_b}}\right)^2 j_{\mathrm{s0}}\left(\frac{2e}{\hbar}\right) \end{aligned} \tag{3.1}$$

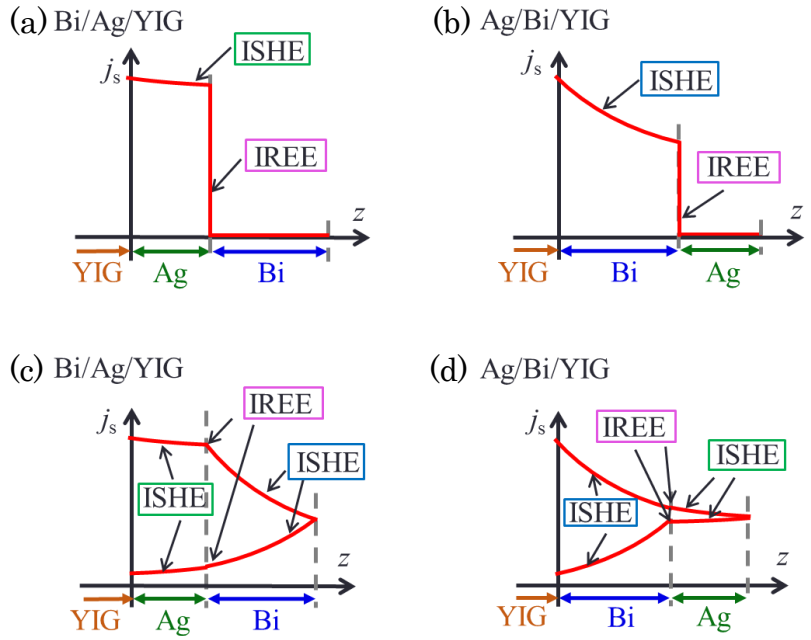

Figure 3-4. Models of spin current flow for $\kappa = 0$ (spin current completely dissipating at Bi/Ag) of (a) Bi/Ag/YIG and (b) Ag/Bi/YIG, and for $\kappa = 1$ (spin current completely transmitted through Bi/Ag) of (c) Bi/Ag/YIG and (d) Ag/Bi/YIG

where *a*, *b* are Bi or Ag, with *a* being a layer directly deposited on the YIG substrate and *b* the other layer, *w* is the sample width (2 mm), θ_{Ag} the spin Hall angle of Ag (0.007 [19]), λ_{Ag} the spin diffusion length of Ag (200 nm [57]), t_{Ag} the thickness of the Ag layer (5 nm), θ_{Bi} the spin Hall angle of Bi (0.02 [26]), λ_{Bi} the spin diffusion length of Bi (8 nm [26]), t_{Bi} the thickness of the Bi layer (7 nm), and λ_{IREE} the Rashba length of the Bi/Ag interface, respectively. The first, second, and third terms of the RHS describe the charge current generated by the ISHE in the layer of *a*, that generated by the IREE at the interface, and that generated by the ISHE in the layer of *b*, respectively. The spin current flowing both forward and back was considered. The double sign in the second term corresponds to the direction of the internal electric field at the Bi/Ag interface and the polarity of the charge current generated by the IREE; the positive sign for the Bi/Ag/YIG, and the negative for the Ag/Bi/YIG.

By applying the result of the charge currents $I_{\mathrm{C,ave}}$ of 300 pA for the Bi/Ag/YIG and 200 pA for the Ag/Bi/YIG to Eq. (3.1), the range of Rashba length was estimated to be 0.07 nm to 0.001 nm. Figure 3-5 shows the Rashba length as a function of $\kappa = [0, 1]$. The author estimated the Rashba length of the Bi/Ag interface to be at least four times smaller than that in the previous studies (~0.3 nm [24,60,61]). Note that the Rashba length can depend on the quality of interface, and, thus, varies between studies. However, in contrast to previous studies, the author substituted the ferrimagnetic insulator for such conductive ferromagnetic materials as NiFe and Fe, which generates spurious signals. The author also took into account contribution of charge current generated by the ISHE. The improvement of measurement samples and the consideration of the spin-charge conversion other than the IREE resulted in the estimation of much smaller Rashba length, which almost corresponds to recent studies of the IREE from the Bi/Ag interface on YIG [41,42].

Tables 3-1 and 3-2 show the intensities of the charge currents generated in the Bi and Ag layers and at the Bi/Ag interface for $\kappa = 0$ ($\lambda_{\mathrm{IREE}} = 0.07$ nm) and $\kappa = 1$ ($\lambda_{\mathrm{IREE}} = 0.001$

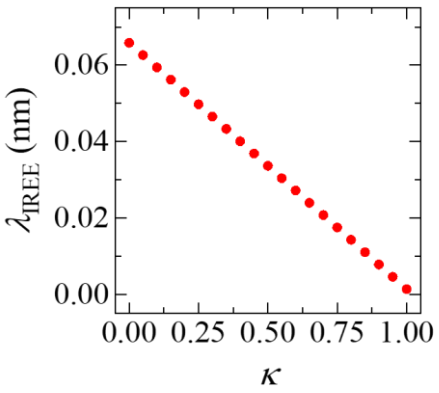

Figure 3-5. Rashba length of Bi/Ag interface λ_{IREE} as a function of transmittance of Bi/Ag interface for $\kappa = [0, 1]$

nm), respectively. For $\kappa = 0$, the majority of the total charge current was generated at the interface in the Bi/Ag/YIG, whereas the charge current in the Bi layer was dominant and that at the interface canceled a part of it in the Ag/Bi/YIG. The influence of the IREE was high compared with the case of $\kappa = 1$. On the other hand, for $\kappa = 1$, almost no charge current was generated at the interface in both samples. In the Bi/Ag/YIG, the charge current generated in the Ag layer adjacent to the YIG was unnaturally large. Therefore, in the range of the Rashba length from 0.001 nm to 0.07 nm, it is estimated that the Rashba length closer to 0.07 nm is more probable. In any case, the result that the Rashba length estimated in this study is smaller than that of the previously reported remains unchanged.

According to the study on the Rashba effect of Bi/Ag with the angle-resolved photoelectron spectroscopy, a spin-split has observed with Bi/Ag(111). Here, among this study and references [24,62], only the Bi/Ag/YIG in this work exhibited Ag(111) peak in X-ray diffraction spectra. In addition, these studies showed similar peaks for the spectra (Bi(003), Bi(012), and Ag(220) peaks), which suggests that the samples in these studies possess similar crystal structure. A question remains how sample quality affects the ratio between the IREE and the ISHE, and the magnitude of the Rashba length.

Table 3-1. Charge current in Bi, Ag layers and Bi/Ag interface, for $\kappa = 0$

Sample	Bi (pA)	Ag (pA)	Bi/Ag (pA)	Total (pA)
Bi/Ag/YIG	0	105	195	300
Ag/Bi/YIG	283	0	-83	200

Table 3-2. Charge current in Bi, Ag layers and Bi/Ag interface, for $\kappa = 1$

Sample	Bi (pA)	Ag (pA)	Bi/Ag (pA)	Total (pA)
Bi/Ag/YIG	103	191	6	300
Ag/Bi/YIG	203	1	-4	200

3.4 Conclusion

The author estimated the Rashba length of the Bi/Ag interface with the following different condition from the previous study; the adoption of a magnetic insulator as a spin injector for the spin pumping, the consideration of charge currents generated by the ISHE in both the Bi

and Ag layers, the introduction of the transmittance of spin current at the Bi/Ag interface, and the employment of two types of samples with direct and reversed stacking orders. In the range of the transmittance from 0 to1, the Rashba length was estimated to be from 0.001 nm to 0.07 nm, about a quarter of the previous study. The fact of the small Rashba length corresponds to recent study. The result implies that introduction of magnetic insulator as a spin injector and the consideration of the ISHE cause the estimation of the small Rashba length. However, it is still a question how sample quality has an influence on the spin-to-charge conversion in the Bi/Ag bilayer [63].

Chapter 4. Spin-charge conversion in Bi/Py bilayer system

4.1 Spin conversion in Bi

Many open questions for the physics of Bi still remain in spintronics, one of which is the fact that the spin Hall angle of Bi is not so large in spite of its high SOC. Despite the lower SOC of Ta, W, Pt, the reported magnitudes of spin-conversion efficiencies of β-Ta [37], β-W [38], Pt [39,40] are larger than the reported spin Hall angles of Bi [25,26]. Other studies employing the spin Seebeck effect show a negligible ISHE signal in Bi(rhombohedral-(111))/YIG [41,42]. The reported spin Hall angles of Bi conducted by the spin pumping method are various; 0.019 in the thick region [25], and 0.02 [26] for the Bi/Py system, and 1.2×10^{-4} for the Bi/YIG system [27]. Figure 4-1 shows spin Hall angles of Bi and other materials as a function of the fourth power of atomic number. When the magnitude of spin Hall angle is proportional to Z^4, the possible spin Hall angle of Bi ($Z = 83$) is 0.12, much larger than the reported value.

The especially remarkable result for the spin Hall angle of Bi is the sign inversion from negative to positive at 2 nm of Bi. The estimated spin Hall angle is 0.019 in the region thicker than 2 nm, and -0.071 in the region thinner than 2 nm [25]. The physics of the change in the polarity of the spin Hall angle of Bi according to its thickness is unclear.

In this study, the author introduced the Bi/Py bilayer system and estimated the spin-charge conversion efficiency of Bi by employing the ST-FMR method [39,51-53]. Numerous Bi/Py devices with different thicknesses of the Bi layer were formed on the same substrate, and

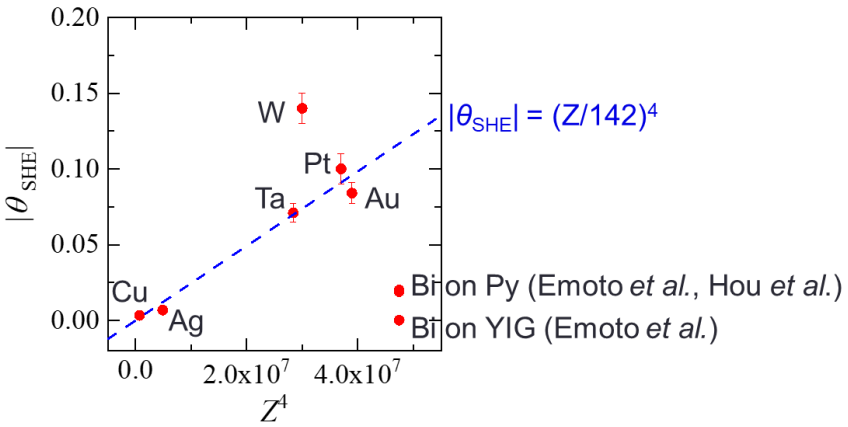

Figure 4-1. Magnitude of spin Hall angles as a function of the fourth power of atomic number. **Data adapted from**: Bi on Py from H. Emoto *et al*., J. Appl. Phys. **115**, 17C507 (2014) [26], and D. Hou *et al*., Appl. Phys. Lett. **101**, 042403 (2012) [25]. Bi on YIG from H. Emoto *et al*., Phys. Rev. B **93**, 174428 (2016) [27]. The others from H. L. Wang *et al*., Phys. Rev. Lett. **112**, 197201 (2014) [19].

the spin-charge conversion efficiency as a function of thickness of Bi was estimated. In addition, after the development of the ST-FMR method, researchers have studied the spin-charge conversion with the ST-FMR for a lot of materials, almost all of which have already estimated with the spin pumping, while the ST-FMR for Bi have not been reported. Therefore, the objective of this study is to estimate the spin-charge conversion efficiency of Bi in the Bi/Py system as a function of the thickness of Bi by introducing the ST-FMR method. In particular, attention is paid to the sign reversal of the conversion efficiency around 2 nm of the Bi.

4.2 Growth and process

Figure 4-2 (a) shows a bilayer sample Bi(1.2 to 10 nm)/Py(5 nm) for this study. The Py layer was grown on a thermally oxidized Si substrate by molecular beam epitaxy, and then the Bi with a wedged structure was grown. The 5-nm MgO and SiO_2 layers were deposited on the top of the substrate in this order, to protect the Bi from oxidation. To measure Bi/Py by the ST-FMR method, this sample should be processed into measurement devices like Fig. 4-2 (b).

Figures 4-3 shows the processes to fabricate measurement devices. First, the surface of the sample was coated with resist, which was etched with electron beam lithography and formed into rectangles (one of them 20 μm × 140 μm in size) (Fig. 4-3 (a)). Besides, Ar ion milling system was applied to remove the region other than those protected by the rectangular resists to expose the surface of the substrate (Fig. 4-3 (b)). Then, the rectangular resists were removed, and another resist was coated and formed into the shape of waveguide with the same process. Note that the regions 5 μm from the ends of the longitudinal direction of the rectangles were not covered with the resist. The Ar ion milling was applied to remove MgO and SiO_2 layers on the regions (Fig. 4-3 (c)). Finally Ti(3 nm) and Au(100 nm) was deposited with electron beam deposition and formed the waveguides (Fig. 4-3 (d)). Here, the exposed Bi/Py and the Au/Ti waveguides were directly

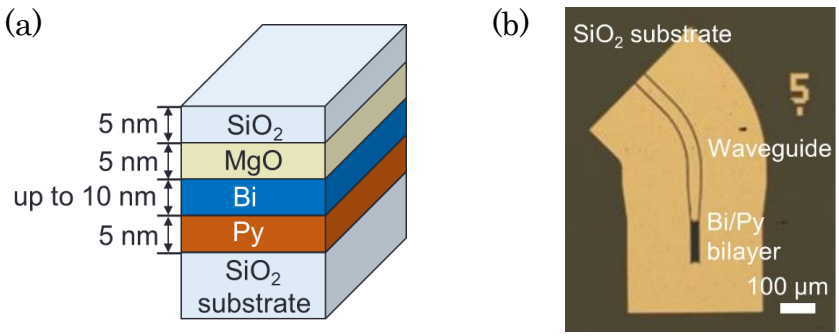

Figure 4-2. (a) Sample stacking of Bi/Py, (b) magnified image of fabricated device, composed by a waveguide (gold region) and a Bi/Py channel (dark region surrounded by the waveguide)

connected. The area of the non-covered region of the Bi/Py channel shown in the position below the centre of Fig. 4-2 (b) was 20 μm × 130 μm in size. Multiple devices with the same waveguides and the channels with different thicknesses of Bi were fabricated on the same substrate.

4.3 Measurement procedure by spin torque-ferromagnetic resonance

Figure 4-4 shows the measurement setup of this study. A circuit consists of a signal generator, a nanovoltmeter, and a bias-tee, and is connected to a device with a GSG probe. In the

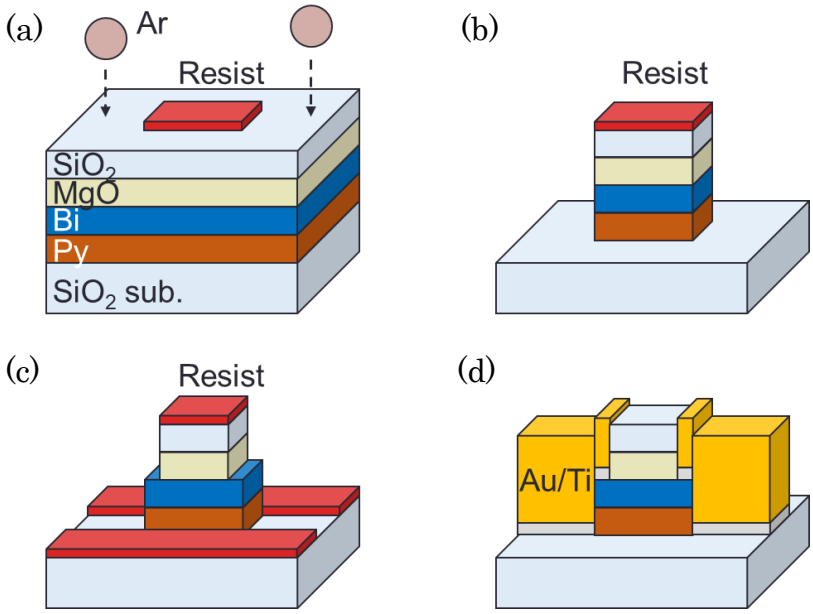

Figure 4-3. Schematic views of the region around a Bi/Py channel while fabricating measurement devices. (a) Ar milling for sample with a rectangular resist, (b) sample after the first milling to expose surface of substrate, (c) sample and resist after the second milling to expose Bi/Py, and (d) completed sample by deposition of Au/Ti waveguide

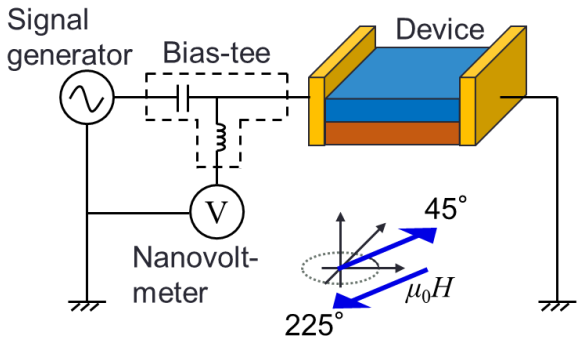

Figure 4-4. Measurement setup of study on Bi/Py, by the spin torque-ferromagnetic resonance

measurement system, an in-plane magnetic field can be applied to the device.

An ac charge current (13 dBm in power) was applied to the device through a capacitor in the bias-tee, and an in-plane magnetic field was applied to the device with a gradual decrease. The direction of the magnetic field was 45° and 225° from the direction of the ac current. The dc voltage, generated by the multiplication of the resistance of the Py layer and the ac charge current, can be measured with the nanovoltmeter by separating itself from the ac charge current, since a capacitor in a bias-tee is open for a dc voltage, whereas an inductor is open for a highly frequent ac charge current. The dc voltage as a function of the magnetic field was analyzed and spin conversion efficiency of Bi was estimated. All the measurement was conducted at room temperature.

4.4 Voltage spectra and spin conversion efficiency

First of all, Py is a ferromagnetic material with negligible magnetocrystallne anisotropy. Hence, the Kittel equation is described as Eq. (2.7) and the spin conversion efficiency η is described as Eq. (2.18), respectively.

Figures 4-5 (a) and (b) shows voltage spectra obtained from the Bi(5 nm)/Py(5 nm) device as a function of magnetic field $\mu_0 H$ at 45° and 225°, respectively. Here, the frequencies of the applied ac current were 7-14 GHz. In the previous study of the IREE in the Py/Ag/Bi system, only negligible signal was detected in the Py(9 nm)/Bi(4 nm) by using the ST-FMR method [64]. Hence, this study was the first case of detecting sizable signals from the Bi/Py system with the ST-FMR. Then, in these graphs, the solid lines on the dots are fittings by Eq. (2.14) for all spectra, which suggests that experimental results correspond to the theoretical picture. When the measuring and analyzing methods were applied to every device, the coefficients S and A in Eq. (2.18) were estimated at every thickness of Bi. By estimating the magnetic resonance fields of the spectra, the ac current frequency as a function of the resonance field $\mu_0 H_{\mathrm{res}}$ was obtained as shown in Fig. 4-5 (c), where the dashed line is a fitting by the Kittel equation Eq. (2.7). The demagnetization field $\mu_0 M_{\mathrm{eff}}$ of the Py on the device with 5-nm-thick Bi layer was estimated to be 0.77 T for a Py g-factor of 2.112 [65]. The reported value of $\mu_0 M_{\mathrm{eff}}$ of 5-nm-thick Py was 0.79 T [66], which suggested that the magnetic property of the Py in this study is comparable to that in previous studies. As a result of estimation of the demagnetization field for every device by using the Kittel equation, the demagnetization field of the Py as a function of the thickness of Bi t_{Bi} was obtained as shown in Fig. 4-5 (d). The estimated demagnetization field of the Py was 0.72 T to 0.82 T, which was comparable to the reported value 0.79 T.

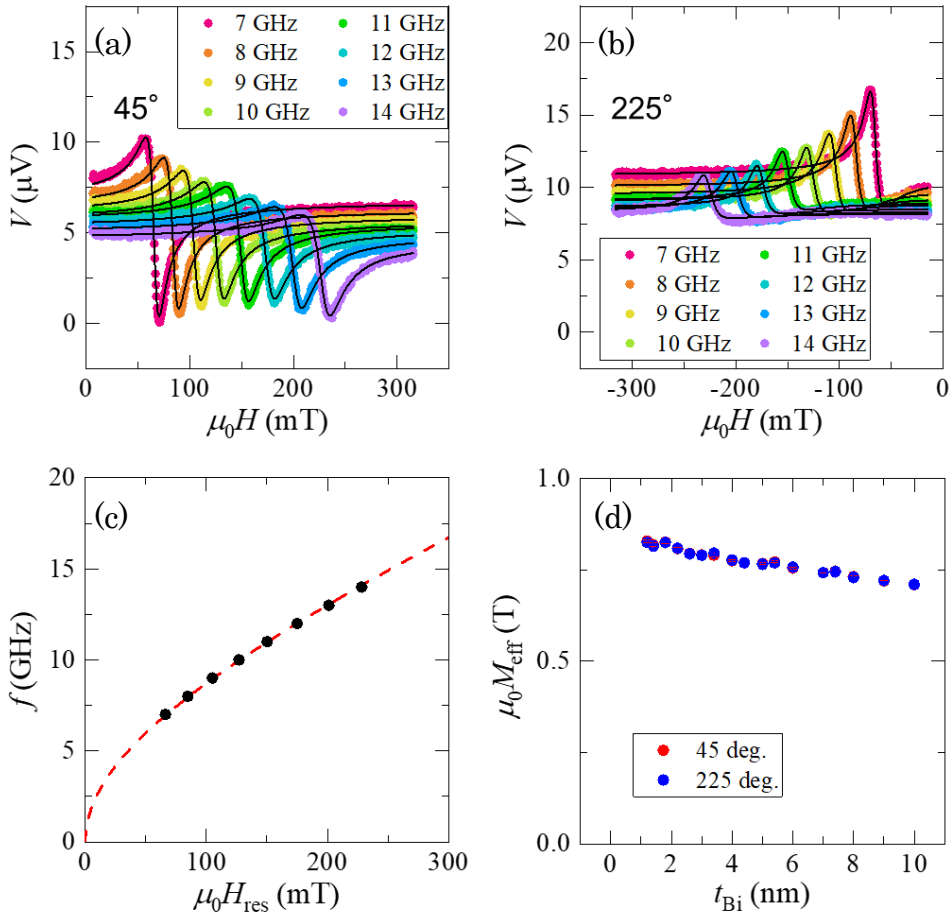

Figure 4-5. Voltage spectra at 7-14 GHz under the application of magnetic field at (a) 45° and (b) 225°, (c) frequency versus resonance field with fitting by the Kittel equation, and (d) demagnetization field versus thickness of Bi

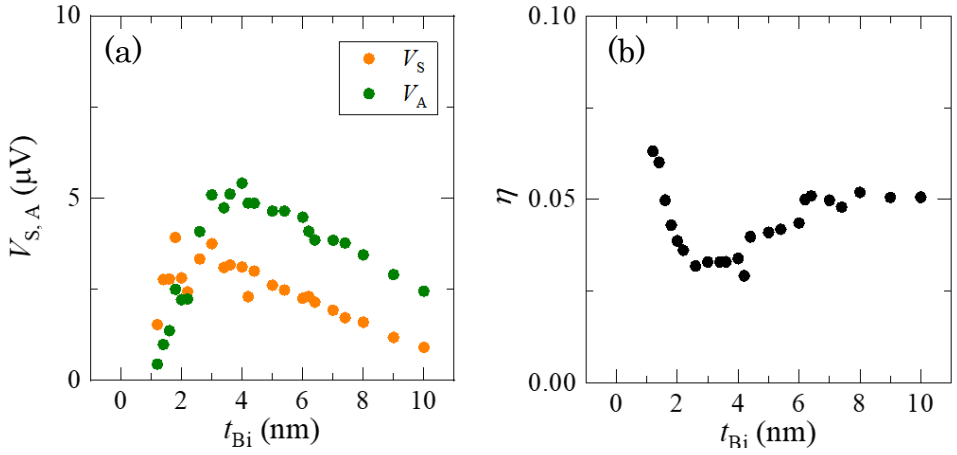

Figure 4-6. (a) Averaged intensities of (anti)symmetric components of voltage spectra as a function of thickness of Bi, and (b) spin-charge conversion efficiency versus thickness of Bi

Figure 4-6 (a) shows amplitudes in the symmetric component $V_S = CS$ and the antisymmetric component $V_A = CA$ in Eq. (2.14) as a function of the thickness of Bi layer, respectively. Note that each amplitude at 45° and 225° were averaged by the same process as in Chapter 3, to erase thermal effects. By applying the voltages and demagnetization field as a function of the thickness of Bi to Eq. (2.18), the spin-charge conversion efficiency η as a function of the thickness of Bi was estimated to be +0.03 to +0.06 in the range of 1.2 nm to 10 nm of the thickness of Bi (see Fig. 4-6 (b)). Here, the saturation magnetization of Py $\mu_0 M_s$ was 0.72 T [66], and a part of the demagnetization field was obtained by linear extrapolation. The result of the spin-charge conversion efficiency versus the thickness of Bi did not correspond to Eq. (2.19) in the region below 2 nm. Figure 4-7 shows the relation between the magnitude of the spin Hall angles and the fourth power of atomic number, with the spin conversion efficiency of the Bi estimated in this study. The magnitude of the conversion efficiency was higher than the spin Hall angle (+0.02) obtained from Bi/Py system by using the spin pumping method [25,26]. However, the estimated spin conversion efficiency from +0.03 to +0.06 was smaller than the probable spin Hall angle of 0.12, which is based on the relation between the magnitude of the spin Hall angle and the atomic number. Finally, unlike the spin Hall angle in the previous study, no sign inversion of the spin-charge conversion efficiency was observed in this range of Bi thickness.

Comparing the spin conversion efficiency and spin Hall angle in the Bi/Py and Bi/YIG systems, it is suggested that, in the spin conversion of Bi, the type of ferromagnetic materials adjacent to Bi affects the spin conversion physics of Bi itself. According to the study of the Bi/YIG

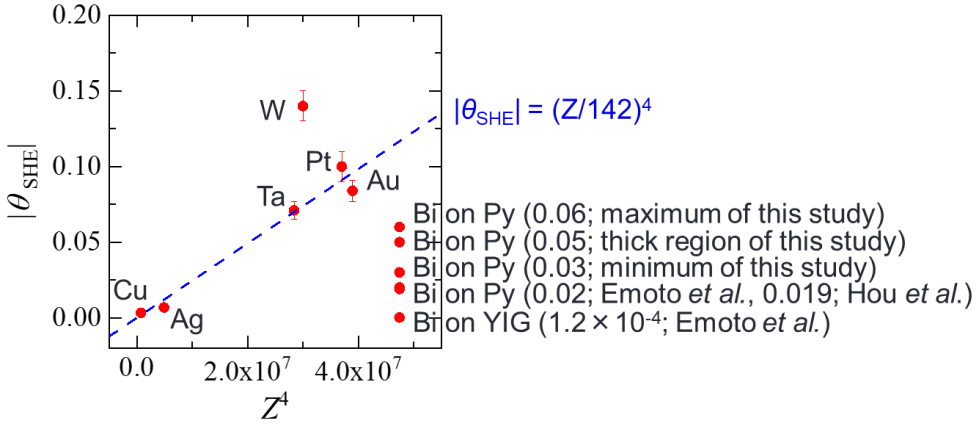

Figure 4-7. Magnitude of spin Hall angles as a function of the fourth power of atomic number, with the spin conversion efficiencies of Bi of the maximum, the thick region, and the minimum, estimated in this study. **Data adapted from**: Bi on Py from H. Emoto *et al.*, J. Appl. Phys. **115**, 17C507 (2014) [26], and D. Hou *et al.*, Appl. Phys. Lett. **101**, 042403 (2012) [25]. Bi on YIG from H. Emoto *et al.*, Phys. Rev. B **93**, 174428 (2016) [27]. The others from H. L. Wang *et al.*, Phys. Rev. Lett. **112**, 197201 (2014) [19].

by using the spin pumping method, the spin Hall angle of Bi was estimated to be 1.2×10^{-4} [27]. In other studies, only negligible voltage was detected in the Bi/YIG system, which was too small to estimate the spin Hall angle of Bi [41,42]. On the other hand, the reported spin Hall angles of Bi in the Bi/Py system are about 0.02 [25,26], which is comparable with the spin conversion efficiency obtained in this study by using the Bi/Py system. It was confirmed that the constants related to spin conversion physics were different by about two orders of magnitude between the Bi/YIG and Bi/Py systems.

4.5 Conclusion

In this study, the author studied the spin conversion in the Bi/Py system by using the ST-FMR method, resulting in the detection of sizable voltage spectra. This is the first case of observing nonnegligible signals from the Bi/Py. By analyzing the voltage spectra, the spin conversion efficiency was estimated to be +0.03 to +0.06 in range of 1.2 nm to 10 nm of the thickness of Bi layer. The reversal of polarity in the spin conversion efficiency in the region around 2 nm of the Bi was not observed. Comparing the spin Hall angles in the Bi/Py, the spin conversion efficiency in this study, and the very small spin Hall angle of Bi/YIG system, the type of ferromagnetic materials for the spin pumping and the ST-FMR was a notable point in Bi-based spintronics [67].

Chapter 5. Spin-charge conversion in bilayer system of highly oriented Bi grown on single-crystalline Fe

5.1 Quality of crystal in Bi

Bi shows various properties due to its peculiar band structure, and several phenomena have been discovered through the study on Bi. In spintronics, Bi has been widely employed as a simple substance [25-27], one layer of an interface like Bi/Ag or Bi/Cu [24-28], topological insulators like $Bi_{1-x}Sb_x$ [29,30], Bi_2Te_2Se [31], $Bi_{2-x}Sb_xTe_{3-y}Se_y$ [32-34], and dopants for host materials [35,36], due to its high SOC. However, in the spin conversion region, Bi has not fully played the expected role. The reported spin Hall angles of Bi was -0.071 to +0.02 [25-27], which was smaller than those of other materials with the smaller SOCs (for example, Pt: 0.10, Ta: -0.071, W: -0.14, Au: 0.084, all the spin Hall angle being estimated with samples deposited on YIGs) [19,20]. Bi exhibits a relatively small spin Hall angle despite the highest SOC among non-radioactive elements. Although the SOC is definitely one of the factors that determine the spin Hall angle, the cause of the small spin Hall angle of Bi is still unclear.

The previous studies introduced polycrystalline Bi and amorphous Bi. The property of Bi, which was caused by its band structure, may not be fully reflected in the spin conversion efficiency, since the qualities of the crystals were far from that of a single-crystal. According to a study on Pt, the scattering mechanism in Pt is different between single-crystalline Pt and polycrystalline Pt [68]. Figure 5-1 shows the relationship between the spin lifetime and the momentum relaxation time for the polycrystalline Pt films and the single-crystalline Pt films. For

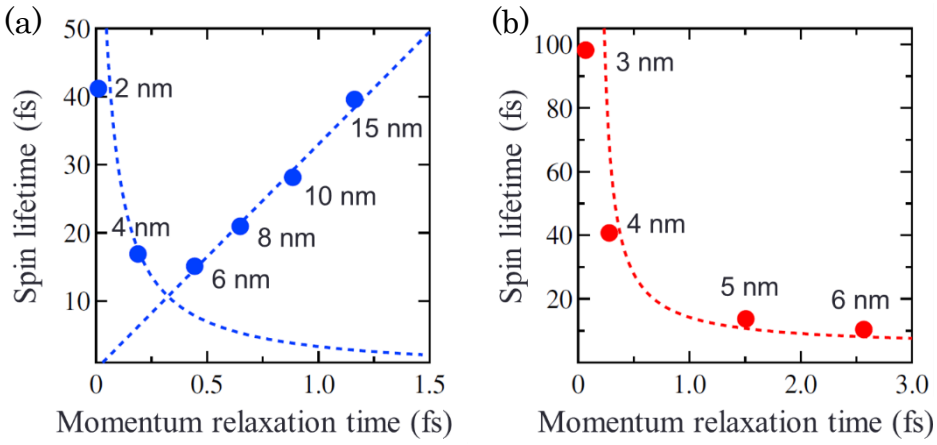

Figure 5-1. The relationship between the spin lifetime and the momentum relaxation time for (a) the polycrystalline Pt and (b) the single crystalline Pt films. **Figures adapted from**: J. Ryu *et al*., Phys. Rev. Lett. **116**, 256802 (2016) [68]. Note that the author has made some additions and modifications to the original figure.

the polycrystalline Py, in the region of 2 to 4 nm, where surface effects like the Rashba effect emerge, the Pt exhibits scattering of the DP mechanism [18], whereas in the region above 6 nm, where surface effect is weakened, the EY mechanism emerges [16,17]. On the other hand, for the single-crystalline Pt, only the DP mechanism emerges in the region of 3 to 6 nm. This study reveals that the mechanism of the spin relaxation is dependent on the quality of crystal. In addition, in addition to Eqs. (2.3) and (2.4), the electron scattering is strongly related to the spin relaxation. Hence, the spin conversion efficiency, which is related to the electron scattering, also possibly varies significantly depending on the quality of the crystal.

In this study, the author introduced highly oriented Bi. It can be grown on single-crystalline Fe, and has higher quality of crystal compared with that of simple polycrystalline Bi and amorphous Bi, which were introduced in the previous studies. The spin conversion efficiency of highly oriented Bi was estimated by the ST-FMR method. A sample of Bi/Fe was processed, and the measurement devices with Bi/Fe bilayer with the different thicknesses of the Bi layer were fabricated on the same substrate. By measuring the multiple devices, the spin-charge conversion efficiency of highly oriented Bi as a function of the thickness of the Bi was estimated.

5.2 Crystal growth and device fabrication

Figure 5-2 shows sample structure of Bi/Fe. Fe (6 nm in thickness) and Bi (up to 10 nm in thickness) were grown on the MgO substrate in this order by molecular beam epitaxy. While growing Bi, temperature of the substrate was maintained at 270 K, and the Bi layer was formed into a wedged structure by closing a shutter gradually while growing. Figure 5-3 shows in-situ images taken by the reflection high-energy electron diffraction, which shows Fe is a single-crystal and Bi is a certain order. To prevent the Bi from oxidizing, both MgO and SiO_2 were grown on the Bi in the order.

Here, for reference, spectra of the XRD measurement were shown obtained from other Bi/Fe and Fe samples, which had the same stacking as the aforementioned main sample. The thicknesses of the Fe and Bi layers were 5 nm and 50 nm. The cooling while growing Bi was NOT performed, which means that the Bi layer of the sample for the XRD and that of the main sample may not necessarily have the same crystal structure. Figure 5-4 (a) shows $\theta/2\theta$ spectra of the Bi(50 nm)/Fe(5 nm) (red line) and Fe(5 nm) (blue line) samples. Fe(002) peak was observed from each sample, and rhombohedral Bi(003) and its equivalent orientations were observed from Bi/Fe. Figure 5-4 (b) shows the result of φ-scan for the MgO (black), the Fe (blue), and the Bi (red) of the Bi/Fe sample. MgO(101) and Fe(101) had four-fold symmetry, and their directions are offset by 45°. No clear in-plane order of Bi was identified. A top view of the sample with the

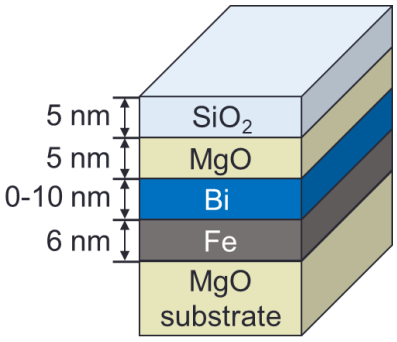

Figure 5-2. Schematic illustration of sample Bi(0-10 nm)/Fe(6 nm), with highly oriented Bi

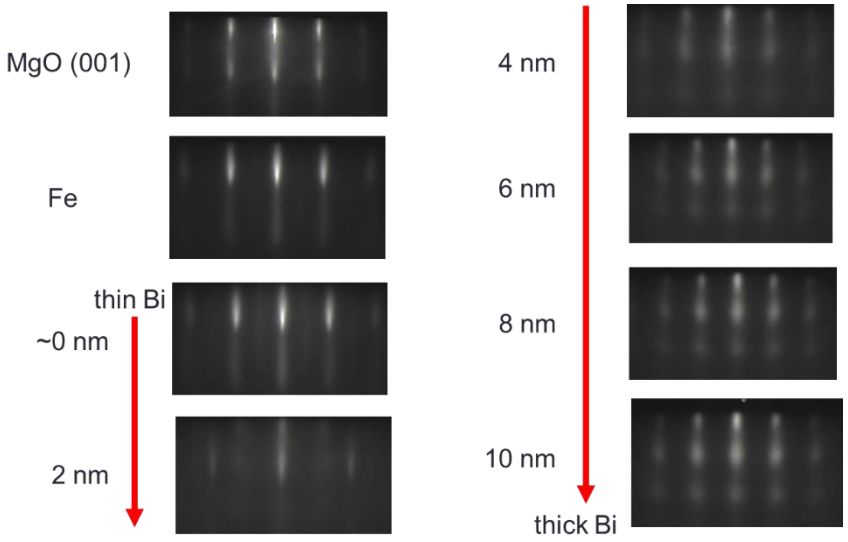

Figure 5-3. In-situ images of reflection high-energy electron diffraction of MgO substrate, Fe, and Bi from ~ 0 nm to 10 nm

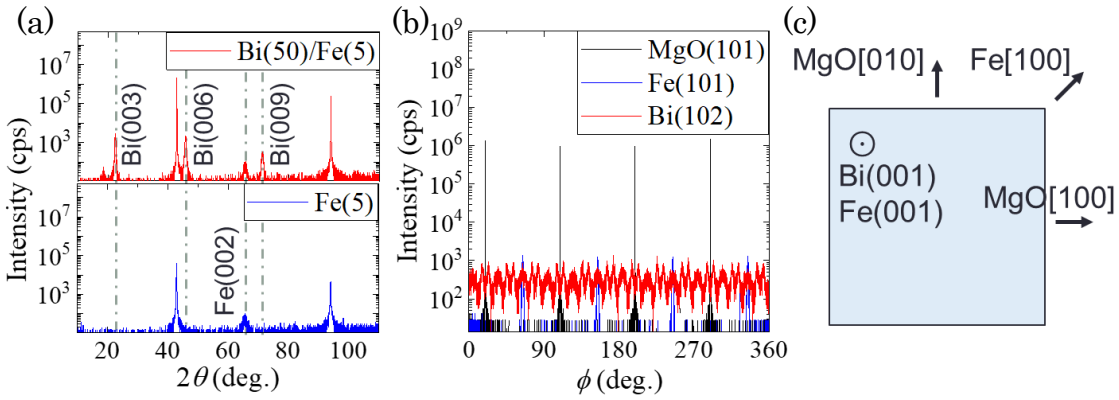

Figure 5-4. (a) Spectra of $\theta/2\theta$ scan for Bi(50 nm)/Fe(5 nm) and Fe(5 nm) measured by X-ray diffraction, (b) spectra of φ-scan for the Bi/Fe, and (c) crystal orientations of the Bi/Fe for Bi and Fe layers and MgO substrate

noteworthy orientations is shown in Fig. 5-4 (c). MgO<100> was perpendicular to the side of the sample, and Fe<100> is oriented 45° rotated with respect to that direction. The offset of Fe-orientation on a MgO(001) substrate has been confirmed by other studies [69].

To conduct the ST-FMR method, Bi/Fe devices shown in Fig. 5-5 were fabricated with the same processes as those in Chapter 4. The Bi/Fe bilayer was formed into rectangular channels of 10 μm × 125 μm in size, by using electron-beam lithography and Ar-ion milling. The channels were joined to waveguides by using the lithography and electron-beam deposition. The non-covered region of the channels was 10 μm × 65 μm. The devices with different thicknesses of Bi was fabricated on the same substrate.

5.3 Measurement procedure

The device was connected to the measurement circuit shown in Fig. 5-6. While an in-plane magnetic field was applied along 45° and 255°, an ac charge current with power of 10 dBm

Figure 5-5. Magnified image of measurement device, consisting of Bi/Fe channel (gray rectangle located below the centre) and waveguide (gold region)

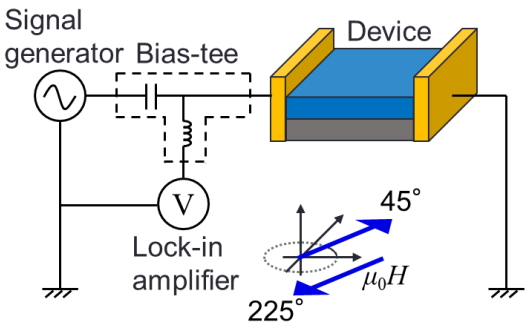

Figure 5-6. Measurement setup of study on Bi/Fe, by the spin torque-ferromagnetic resonance

was applied to the device by using a signal generator. The direction of 45° and 255° were along Fe[100] and Fe[-100], which means the magnetic field was applied along easy axes of Fe. Due to the multiplication of the ac charge current and the time-dependent resistance of the Fe layer, devices generated dc voltage, which was detected by a lock-in amplifier. By analyzing components of the dc spectra, the spin-charge conversion efficiency of the Bi was estimated. A series of measurements was performed on every device. The spin conversion efficiency as a function of the thickness of the Bi was estimated with the ST-FMR method. All measurement was conducted at room temperature.

5.4 Voltage spectra and spin conversion in highly oriented Bi

Figures 5-7 (a) and (b) show observed voltage spectra at 13-20 GHz obtained from Bi(5 nm)/Fe(6 nm). The external magnetic field was applied along 45° and 225°, respectively. Solid lines were fittings to Eq. (2.14) for all spectra, which coincided with the measured data. By estimating the resonance field of each spectrum, the frequency as a function of the resonance field was obtained for the Bi(5 nm)/Fe device under the application of magnetic field at 45° (see Fig. 5-8). The dashed line was a fitting by the Kittel equation with the magnetocrystalline anisotropy under the application of magnetic field along Fe<100> [70], which is described as

$$f_0 = \frac{\gamma}{2\pi}\sqrt{(\mu_0 H_{\mathrm{res}} + \mu_0 H_{\mathrm{a}})(\mu_0 H_{\mathrm{res}} + \mu_0 H_{\mathrm{a}} + \mu_0 M_{\mathrm{eff}})}, \tag{5.1}$$

where $\mu_0 H_{\mathrm{a}}$ is an anisotropic field. Here, the g-factor of Fe was 2.089 [71]. The anisotropic field and the demagnetization field were estimated to be 50 mT and 1.8 T, respectively.

Figure 5-9 (a) shows the amplitudes of the symmetric component V_{S} and the antisymmetric component V_{A} in Eq. (2.14) as a function of the thickness of Bi, respectively. Here, each amplitude obtained from 45° and 225° were averaged by applying the same calculation as in Chapters 3 and 4 to erase thermal effects. By applying the effect of the mangetocrystalline anisotropy to Eq. (2.17) [39,53,72], the spin-charge conversion efficiency of the Bi in this system is described as

$$\eta = \frac{S}{A}\frac{e\mu_0 M_{\mathrm{S}} t_{\mathrm{Fe}} t_{\mathrm{Bi}}}{\hbar}\sqrt{\frac{\mu_0 H_{\mathrm{res}} + \mu_0 H_{\mathrm{a}} + \mu_0 M_{\mathrm{eff}}}{\mu_0 H_{\mathrm{res}} + \mu_0 H_{\mathrm{a}}}}. \tag{5.2}$$

The conversion efficiency as a function of the thickness of Bi was estimated to be -0.01 to +0.36 as shown in Fig. 5-9 (b). This result mostly satisfied Eq. (2.19), except that it did not fully saturate in the thick region. The magnitude of spin-charge conversion efficiency was higher than that of other materials measured by the ST-FMR (Pt: 0.056 [39,40], β-Ta: -0.12 [37], β-W: -0.33 [38]),

and the spin Hall angle of Bi measured by the spin pumping (~ 0.02 [25,26]). Moreover, the conversion efficiency in the thick region was three times as large as that of the possible spin Hall angle of the Bi: 0.12 (see Fig. 5-10). Although the spin conversion efficiency cannot directly

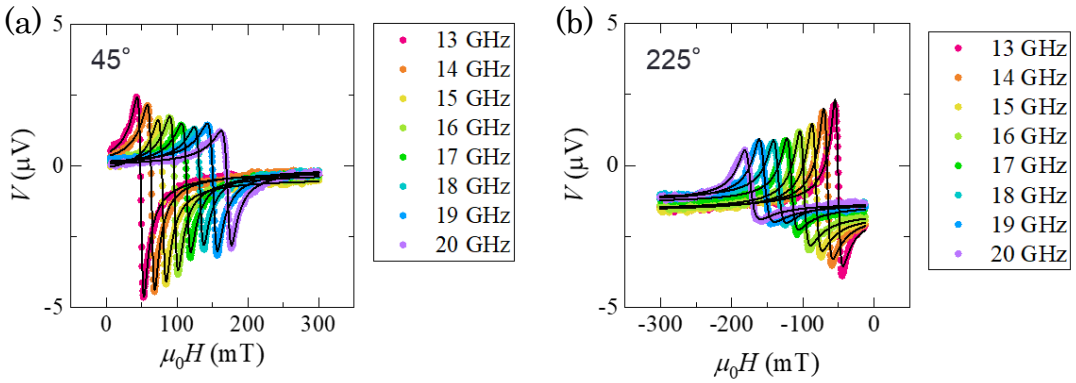

Figure 5-7. Voltage spectra at 13-20 GHz obtained from Bi/Fe, under the application of magnetic field at (a) 45° and (b) 225°

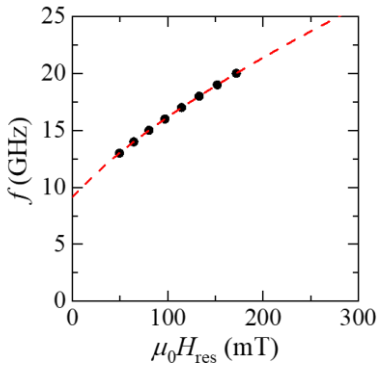

Figure 5-8. The frequency as a function of the resonance field with a fitting described by the Kittel equation with the magnetocrystalline anisotropy of Fe

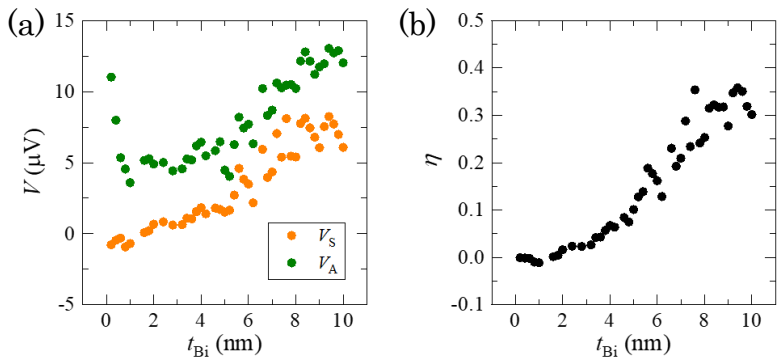

Figure 5-9. (a) Amplitudes of symmetric and antisymmetric components of voltage spectra as a function of the thickness of highly oriented Bi, and (b) the spin-charge conversion efficiency as a function of the thickness of highly oriented Bi

compared with the spin Hall angle acculately, and it is not necessarily appropriate to compare the result of this study with the highly oriented Bi with the results of other studies with polycrystalline materials, it is significant to note that the huge spin conversion efficiency was actually estimated. This gigantic conversion efficiency suggests that the quality of crystal has a great influence on the spin-charge conversion physics.

In addition, the negative spin conversion efficiency was estimated in the region of 0 to 1.0 nm. According to D. Hou *et al*., the spin Hall angle of Bi below 2.0 nm was -0.071 and that above 2.0 nm was +0.019, respectively [25]. The physics of sign reversal in the conversion efficiency has been unclear. The result of this study was partly consistent to the previous study in the polarity of spin conversion efficiency in the thin region.

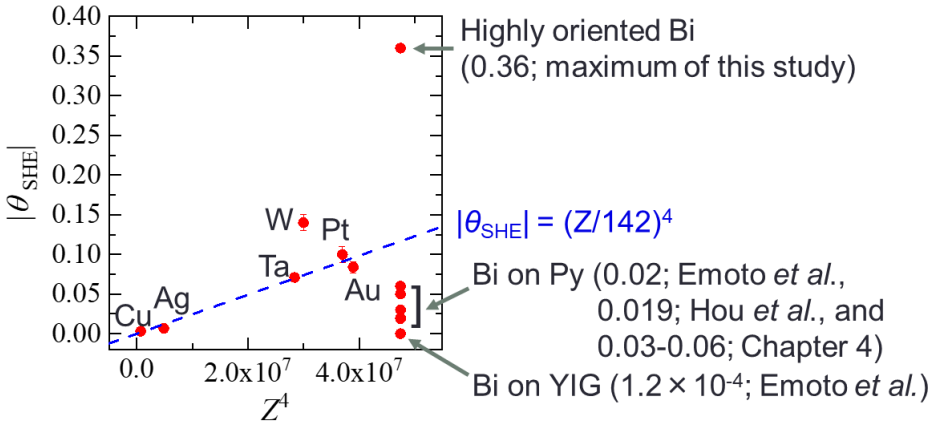

Figure 5-10. Magnitude of spin Hall angles as a function of the fourth power of atomic number, with the spin conversion efficiencies of the highly oriented Bi of the maximum estimated in this study. **Data adapted from**: Bi on Py from H. Emoto *et al*., J. Appl. Phys. **115**, 17C507 (2014) [26], D. Hou *et al*., Appl. Phys. Lett. **101**, 042403 (2012) [25], and Chap. 4. Bi on YIG from H. Emoto *et al*., Phys. Rev. B **93**, 174428 (2016) [27]. The others from H. L. Wang *et al*., Phys. Rev. Lett. **112**, 197201 (2014) [19].

5.5 Conclusion

The author studied the spin conversion of the highly oriented Bi on the single-crystalline Fe by using the ST-FMR method. Voltage spectra were detected from multiple devices, and the spin-charge conversion efficiency as a function of the thickness of Bi was estimated to be -0.01 to +0.36. In the thick region, the sizable conversion efficiency was estimated, since the quality of crystal has a great influence on the spin-charge conversion physics. In the thin region, the negative spin-charge conversion efficiency was estimated, which was consistent to the previous study [73].

Chapter 6. Conclusion of the dissertation

In this dissertation, the author studied on the spin-charge conversion in Bi-based systems, that is, the Bi/Ag interface, the Bi/Py bilayer, and the highly oriented Bi grown on the single-crystalline Fe. Although unresolved problems still remain in both the IREE at the interface and the SHE and ISHE in bulks, the results of this dissertation have made some progress in studies of spintronics.

The results of each chapter are summarized in the following.

◆ **Chapter 3. Inverse Rashba-Edelstein effect in Bi/Ag and Ag/Bi**

- ✓ The Rashba length of the Bi/Ag bilayer system was estimated by adopting insulating YIG as a magnetic material for the spin pumping, introducing a model of spin flow in the bilayer, and measuring both the Bi/Ag/YIG and the Ag/Bi/YIG.
- ✓ The Rashba length of the Bi/Ag was estimated to be 0.001 nm to 0.07 nm, which was much smaller than that of the reported.
- ✓ The result of the small Rashba length is consistent with the recent studies, in which only negligible signals were observed from the Bi/Ag.

◆ **Chapter 4. Spin-charge conversion in Bi/Py bilayer system**

- ✓ The spin-charge conversion in the Bi/Py system due to the SHE was estimated by the ST-FMR method.
- ✓ The spin-charge conversion efficiency was estimated to be +0.03 to +0.06 in the region of 1.2 nm to 10 nm in the thickness of Bi layer.
- ✓ The fact has been revealed that the ferromagnetic materials adjacent to Bi have an influence on the spin conversion physics of the Bi.

◆ **Chapter 5. Spin-charge conversion in bilayer system of highly oriented Bi grown on single-crystalline Fe**

- ✓ The spin-charge conversion in a system of the highly oriented Bi grown on the single-crystalline Fe was estimated by the ST-FMR method.
- ✓ The spin-charge conversion efficiency was estimated to be -0.01 to +0.36; the gigantic spin conversion efficiency in the thick region and the negative spin conversion efficiency in the thin region were estimated.
- ✓ The improvement of the quality of crystal in Bi has a great influence on the spin-conversion physics.

Reference

[1] M. N. Baibich, J. M. Broto, A. Fert, F. Nguyen Van Dau, F. Petroff, P. Etienne, G. Creuzet, A. Friederich, and J. Chazelas, Phys. Rev. Lett. **61**, 2472 (1988).

[2] G. Binasch, P. Grünberg, F. Saurenbach, and W. Zinn, Phys. Rev. B **39**, 4828 (1989).

[3] J. C. Slonczewski, J. of Magn. and Magn. Mater. **159**, L1 (1996).

[4] L. Berger, Phys. Rev. B **54**, 9353 (1996).

[5] E. B. Myers, D. C. Ralph, J. A. Katine, R. N. Louis, and R. A. Buhrman, Science **285**, 867 (1999).

[6] S. Murakami, N. Nagaosa, and S. C. Zhang, Science **301**, 1348 (2003).

[7] J. Sinova, D. Culcer, Q. Niu, N. A. Sinitsyn, T. Jungwirth, and A. H. MacDonald, Phys. Rev. Lett. **92**, 126603 (2004).

[8] Y. K. Kato, R. C. Myers, A. C. Gossard, and D. D. Awschalom, Science **306**, 1910 (2004).

[9] E. Saitoh, M. Ueda, H. Miyajima, and G. Tatara, Appl. Phys. Lett. **88**, 182509 (2006).

[10] T. Kimura, Y. Otani, T. Sato, S. Takahashi, and S. Maekawa, Phys. Rev. Lett. **98**, 156601 (2007).

[11] S. O. Valenzuela, and M. Tinkham, Nature **442**, 176 (2006).

[12] Y. A. Bychkov, and E. I. Rashba, JETP Lett. **39**, 78 (1984).

[13] V. M. Edelstein, Solid State Commun. **73**, 233 (1990).

[14] K. Shen, G. Vignale, and R. Raimondi, Phys. Lev. Lett. **112**, 96601 (2014).

[15] Y. Otani, M. Shiraishi, A. Oiwa, E. Saitoh and M. Murakami, Nature Physics **13**, 829 (2017).

[16] Y. Yafet, Phys. Rev. **85**, 478 (1952).

[17] R. J. Elliott, Phys. Rev. **96**, 266 (1954).

[18] M. I. D'yakonov, and V. I. Perel', Sov. Phys. JETP **33**, 1053 (1971).

[19] H. L. Wang, C. H. Du, Y. Pu, R. Adur, P. C. Hammel, and F. Y. Yang, Phys. Rev. Lett. **112**, 197201 (2014).

[20] C. Du, H. Wang, F. Yang, and P. C. Hammel, Phys. Rev. B **90**, 140407(R) (2014).

[21] K. V. Shanavas, Z. S. Popović, and S. Satpathy, Phys. Rev. B **90**, 165108 (2014).

[22] F. Herman, C. D. Kuglin, K. F. Cuff, and R. L. Kortum, Phys. Rev. Lett. **11**, 541 (1963).

[23] C. R. Ast, J. Henk, A. Ernst, L. Moreschini, M. C. Falub, D. Pacilé, P. Bruno, K. Kern, and M. Grioni, Phys. Rev. Lett. **98**, 186807 (2007).

[24] J. C. Rojas Sánchez, L. Vila, G. Desfonds, S. Gambarelli, J. P. Attané, J. M. De Teresa, C. Magén, and A. Fert, Nature Commun. **4**, 2944 (2013).

[25] D. Hou, Z. Qiu, K. Harii, Y. Kajiwara, K. Uchida, Y. Fujikawa, H. Nakayama, T. Yoshino, T. An, K. Ando, X. Jin, and E. Saitoh, Appl. Phys. Lett. **101**, 42403 (2012).

[26] H. Emoto, Y. Ando, E. Shikoh, Y. Fuseya, T. Shinjo, and M. Shiraishi, J. Appl Phys. **115**,

17C507 (2014).
[27] H. Emoto, Y. Ando, G. Eguchi, R. Ohshima, E. Shikoh, Y. Fuseya, T. Shinjo, and M. Shiraishi, Phys. Rev. B **93**, 174428 (2016).
[28] M. Isasa, M. C. Martínez-Velarte, E. Villamor, C. Magén, L. Morellón, J. M. De Teresa, M. R. Ibarra, G. Vignale, E. V. Chulkov, E. E. Krasovskii, L. E. Hueso, and F. Casanova, Phys. Rev. B **93**, 14420 (2016).
[29] D. Hsieh, D. Qian, L. Wray, Y. Xia, Y. S. Hor, R. J. Cava, and M. Z. Hasan, Nature **452**, 970 (2008).
[30] A. Nishide, A. A. Taskin, Y. Takeichi, T. Okuda, A. Kakizaki, T. Hirahara, K. Nakatsuji, F. Komori, Y. Ando, and I. Matsuda, Phys. Rev. B **81**, 041309(R) (2010).
[31] Z. Ren, A. A. Taskin, S. Sasaki, K. Segawa, and Y. Ando, Phys. Rev. B **82**, 241306(R) (2010).
[32] A. A. Taskin, Z. Ren, S. Sasaki, K. Segawa, and Y. Ando, Phys. Rev. Lett. **107**, 16801 (2011).
[33] Z. Ren, A. A. Taskin, S. Sasaki, K. Segawa, and Y. Ando, Phys. Rev. B **84**, 165311 (2011).
[34] Yu. Ando, T. Hamasaki, T. Kurokawa, F. Yang, M. Novak, S. Sasaki, K. Segawa, Yo. Ando, and M. Shiraishi, Nano Lett. **14**, 6226 (2014).
[35] Y. Niimi, Y. Kawanishi, D. H. Wei, C. Deranlot, H. X. Yang, M. Chshiev, T. Valet, A. Fert, and Y. Otani, Phys. Rev. Lett. **109**, 156602 (2012).
[36] F. Rortais, S. Lee, R. Ohshima, S. Dushenko, Y. Ando, and M. Shiraishi, Appl. Phys. Lett. **113**, 122408 (2018).
[37] L. Liu, C.-F. Pai, Y. Li, H. W. Tseng, D. C. Ralph, and R. A. Buhrman, Science **336**, 555 (2012).
[38] C.-F. Pai, L. Liu, Y. Li, H. W. Tseng, D. C. Ralph, and R. A. Buhrman, Appl. Phys. Lett. **101**, 122404 (2012).
[39] L. Liu, T. Moriyama, D. C. Ralph, and R. A. Buhrman, Phys. Rev. Lett. **106**, 36601 (2011).
[40] A. Ganguly, K. Kondou, H. Sukegawa, S. Mitani, S. Kasai, Y. Niimi, Y. Otani, and A. Barman, Appl. Phys. Lett. **104**, 72405 (2014).
[41] D. Yue, W. Lin, J. Li, X. Jin, and C. L. Chien, Phys. Rev. Lett. **121**, 37201 (2018).
[42] D. Yue, W. Lin, and C. L. Chien, APL Mater. **9**, 50904 (2021).
[43] C. Kittel, Phys. Rev. **73**, 155 (1948).
[44] L. Landau, and E. Lifshits, Phys. Zeitsch. der Sow. **153**, 8 (1935).
[45] T. L. Gilbert, Phys. Rev. **100**, 1243 (1955).
[46] R. H. Silsbee, A. Janossy, and P. Monod, Phys. Rev. B **19**, 4382 (1979).
[47] Y. Tserkovnyak, A. Brataas, and G. E. W. Bauer, Phys. Rev. B **66**, 224403 (2002).
[48] K. Ando, S. Takahashi, J. Ieda, Y. Kajiwara, H. Nakayama, T. Yoshino, K. Harii, Y. Fujikawa, M. Matsuo, S. Maekawa, and E. Saitoh, J. Appl. Phys. **109**, 103913 (2011).
[49] B. F. Miao, S. Y. Huang, D. Qu, and C. L. Chien, Phys. Rev. Lett. **111**, 66602 (2013).

[50] A. Tsukahara, Y. Ando, Y. Kitamura, H. Emoto, E. Shioh, M. P. Delmo, T. Shinjo and M. Shiraishi, Phys. Rev. B **89**, 235317 (2014).
[51] A. A. Tulapurkar, Y. Suzuki, A. Fukushima, H. Kubota, H. Maehara, K. Tsunekawa, D. D. Djayaprawira, N. Watanabe, and S. Yuasa, Nature **438**, 339 (2005).
[52] J. C. Sankey, P. M. Braganca, A. G. F. Garcia, I. N. Krivorotov, R. A. Buhrman, and D. C. Ralph, Phys. Rev. Lett. **96**, 227601 (2006).
[53] J. C. Sankey, Y.-T. Cui, J. Z. Sun, J. C. Slonczewski, R. A. Buhrman, and D. C. Ralph, Nature Physics **4**, 67 (2008).
[54] J. N. Kupferschmidt, S. Adam, and P. W. Brouwer, Phys. Rev. B **74**, 134416 (2006).
[55] S. Zhang, P. M. Levy, and A. Fert, Phys. Rev. Lett. **88**, 236601 (2002).
[56] K. Kondou, H. Sukegawa, S. Mitani, K. Tsukagoshi, and S. Kasai, Appl. Phys. Express **5**, 73002 (2012).
[57] T. Kimura, and Y. Otani, Phys. Rev. Lett. **99**, 196604 (2007).
[58] L. Chen, S. Ikeda, F. Matsukura, and H. Ohno, Appl. Phys. Express **7**, 13002 (2014).
[59] A. Azevedo, R. O. Cunha, F. Estrada, O. Alves Santos, J. B. S. Mendes, L. H. Vilela-Leão, R. L. Rodríguez-Suárez, and S. M. Rezende, Phys. Rev. B **92**, 24402 (2015).
[60] S. Sangiao, J. M. De Teresa, L. Morellon, I. Lucas, M. C. Martinez-Velarte,and M. Viret, Appl. Phys. Lett. **106**, 172403 (2015).
[61] A. Nomura, T. Tashiro, H. Nakayama, and K. Ando, Appl. Phys. Lett. **106**, 212403 (2015).
[62] H. J. Zhang, S. Yamamoto, B. Gu, H. Li, M. Maekawa, Y. Fukaya, and A. Kawasuso, Phys. Rev. Lett. **114**, 166602 (2015).
[63] M. Matsushima, Y. Ando, S. Dushenko, R. Ohshima, R. Kumamoto, T. Shinjo, and M. Shiraishi, Appl. Phys. Lett. **110**, 72404 (2017).
[64] M. B. Jungfleisch, W. Zhang, J. Sklenar, W. Jiang, J. E. Pearson, J. B. Ketterson, and A. Hoffmann, Phys. Rev. B **93**, 224419 (2016).
[65] J. M. Shaw, H. T. Nembach, T. J. Silva, and C. T. Boone, J. Appl. Phys. **114**, 243906 (2013).
[66] S. Hirayama, S. Mitani, Y. Otani, and S. Kasai, Appl. Phys. Express **11**, 13002 (2018).
[67] M. Matsushima, S. Miwa, S. Sakamoto, T. Shinjo, R. Ohshima, Y. Ando, Y. Fuseya, and M. Shiraishi, Appl. Phys. Lett. **117**, 42407 (2020).
[68] J. Ryu, M. Kohda, and J. Nitta, Phys. Rev. Lett. **116**, 256802 (2016).
[69] Y. Kasatani, and Y. Nozaki, J. Magn. Soc. Jpn. **39**, 221 (2015).
[70] O. Kohomoto, and C. Alexander, Jpn. J Appl. Phys. **31**, 2101 (1992).
[71] Z. Frait, and R. Gemperle, Journal de Physique Colloques **32 (C1)**, C1-541 (1971).
[72] C. Guillemard, S. Petit-Watelot, S. Andrieu, and J. C. Rojas-Sanchez, Appl. Phys. Lett. **113**, 262404 (2018).
[73] M. Matsushima *et al*, in preparation.

Publication list

As first author

1. M. Matsushima, Y. Ando, S. Dushenko, R. Ohshima, R. Kumamoto, T. Shinjo, and M. Shiraishi, "Quantitative investigation of the inverse Rashba-Edelstein effect in Bi/Ag and Ag/Bi on YIG", Applied Physics Letters **110**, 072404 (2017).

2. M. Matsushima, S. Miwa, S. Sakamoto, T. Shinjo, R. Ohshima, Y. Ando, Y. Fuseya, and M. Shiraishi, "Sizable spin-transfer torque in the Bi/$Ni_{80}Fe_{20}$ bilayer film", Applied Physics Letters **117**, 042407 (2020).

As a co-author

1. M. Aoki, E. Shigematsu, M. Matsushima, R. Ohshima, S. Honda, T. Shinjo, M. Shiraishi and Y. Ando, "In-plane spin-orbit torque magnetization switching and its detection using the spin rectification effect at sub-GHz frequencies", Physical Review B **102**, 174442 (2020).

2. M. Aoki, E. Shigematsu, M. Matsushima, R. Ohshima, S. Honda, T. Shinjo, M. Shiraishi and Y. Ando, "Enhancement of low-frequency spin-orbit-torque ferromagnetic resonance signals by frequency tuning observed in Pt/Py, Pt/Co, and Pt/Fe bilayers", AIP Advances **11**, 025206 (2021).

Presentations at international conference

1. M. Matsushima, S. Dushenko, R. Ohshima, Y. Ando, T. Shinjo, and M. Shiraishi, "Investigation of the inverse Rashba-Edelstein effect in Bi/Ag/YIG and Ag/Bi/YIG", 9th International Conference on Physics and Applications of Spin-Related Phenomena in Solids, P2-26, Kobe Japan, Aug. 8-11, 2016. [Poster]

2. M. Matsushima, S. Dushenko, R. Ohshima, Y. Ando, T. Shinjo, and M. Shiraishi, "Investigation of spin to charge conversion at Bi/Ag interface on yttrium iron garnet", 61st Annual Conference on Magnetism and Magnetic Materials, FB-03, New Orleans USA, Oct. 31 - Nov. 4, 2016. [Oral]

3. M. Matsushima, Y. Ando, S. Dushenko, T. Kawabe, T. Shinjo, S. Miwa, and M. Shiraishi, "Inverse spin Hall effect in single-crystal bismuth", Spintech 9, Fukuoka Japan, Jun. 4-8, 2017. [Poster]

4. M. Matsushima, Y. Ando, S. Dushenko, T. Kawabe, T. Shinjo, S. Miwa, and M. Shiraishi, “Inverse spin Hall effect in highly oriented bismuth”, 62nd Annual Conference on Magnetism and Magnetic Materials, EB-04, Pittsburgh USA, Nov. 6-10, 2017. [Oral]

5. M. Matsushima, Y. Ando, R. Ohshima, S. Dushenko, E. Shigematsu, T. Kawabe, T. Shinjo, S. Miwa, M. Shiraishi, “Spin Hall effect in highly oriented bismuth by using spin-torque ferromagnetic resonance”, Materials Research Meeting 2019, E2-11-O08, Yokohama Japan, Dec. 10-14, 2019. [Oral]

Presentations at domestic conference

1. M. Matsushima, S. Dushenko, R. Ohshima, Y. Ando, T. Shinjo, and M. Shiraishi, “Observation of inverse Rashba-Edelstein effect in Bi/Ag and Ag/Bi interfaces with ferromagnetic insulator”, 平成 27 年度スピン変換年次報告会, PS-13, 仙台, 1 月 7-8 日, 2016. [Poster]

2. M. Matsushima, S. Dushenko, R. Ohshima, Y. Ando, T. Shinjo, and M. Shiraishi, “Investigation of the inverse Rashba-Edelstein effect in Bi/Ag and Ag/Bi on ferromagnetic insulator”, 第 63 回応用物理学会春季学術講演会, 21p-W241-9, 東京, 3 月 19-22 日, 2016. [Oral]

3. 松島真之, 安藤裕一郎, Sergey Dushenko, 河辺健志, 新庄輝也, 三輪真嗣, 白石誠司, “単結晶 Bi における逆スピンホール効果”, 第 21 回スピン工学の基礎と応用, A-3, 札幌, 12 月 12-13 日, 2016. [Oral]

4. M. Matsushima, Y. Ando, S. Dushenko, K. Kawabe, T. Shinjo, S. Miwa, and M. Shiraishi, “Spin to charge conversion in single-crystal bismuth”, 平成 28 年度スピン変換年次報告会, PF-41, 東京, 3 月 2-3 日, 2017. [Poster]

5. 松島真之, 安藤裕一郎, Sergey Dushenko, 河辺健志, 新庄輝也, 三輪真嗣, 白石誠司, “単結晶 Bi を用いたスピン流-電流変換”, 日本物理学会 第 72 回年次大会, 20pC24-5, 大阪, 3 月 17-20 日, 2017. [Oral]

6. M. Matsushima, Y. Ando, S. Dushenko, T. Kawabe, T. Shinjo, S. Miwa, and M. Shiraishi, “Detection of spin-charge conversion in highly oriented bismuth grown by molecular beam epitaxy”, 平成 29 年度スピン変換研究会, P-35, 大阪, 9 月 11-12 日, 2017. [Poster]

7. M. Matsushima, Y. Ando, S. Dushenko, T. Kawabe, T. Shinjo, S. Miwa, and M. Shiraishi, “Bi 高配向膜を用いた逆スピンホール効果”, 応用物理学会関西支部 平成 29 年度第 2 講演会, P-16, 京都, 11 月 17 日, 2017. [Poster]

8. M. Matsushima, Y. Ando, S. Dushenko, T. Kawabe, T. Shinjo, S. Miwa, and M. Shiraishi, “Inverse spin Hall effect in highly oriented bismuth grown by molecular beam epitaxy”, 平成 29 年度スピン変換年次報告会, P-28, 京都, 3 月 12-13 日, 2018. [Poster]

9. M. Matsushima, Y. Ando, R. Ohshima, S. Dushenko, E. Shigematsu, T. Kawabe, T. Shinjo, S. Miwa, M. Shiraishi, “Spin-charge conversion in highly oriented bismuth using spin-torque ferromagnetic resonance”, 第 66 回応用物理学会春季講演会, 11a-M101-4, 東京, 3 月 9-12 日, 2019. [Oral]

10. 松島真之, 安藤裕一郎, 大島諒, Sergey Dushenko, 重松英, 河辺健志, 新庄輝也, 三輪真嗣, 白石誠司, “Spin-charge conversion via highly oriented bismuth”, 平成 30 年度スピン変換年次報告会, PS-24, 仙台, 3 月 18-19 日, 2019. [Poster]

11. 松島真之, Sergey Dushenko, 伏屋雄紀, 河辺健志, 三輪真嗣, 重松英, 大島諒, 新庄輝也, 大島諒, 安藤裕一郎, 白石誠司, “高配向 Bi を用いたスピントルク強磁性共鳴法によるスピン変換”, 日本物理学会 2019 年秋季大会, 10pD10-6, 岐阜, 9 月 10-13 日, 2019. [Oral]

Acknowledgement

These studies have been conducted in and discussed with Shiraishi laboratory in Department of Electronic Science and Engineering, Kyoto University, Miwa laboratory in the Institute for Solid State Physics, the University of Tokyo, and other collaborators. In particular, Bi/Py and Bi/Fe samples studied in Chapter 4 and 5 were grown in Miwa laboratory. These studies were supported by a Grant-in-Aid for Scientific Research from the Ministry of Education, Culture, Sports, Science and Technology (MEXT) of Japan, Innovative Area “Nano Spin Conversion Science” (No. 26103003), Scientific Research (S) “Semiconductor Spincurrentronics” (No. 16H0633), Scientific Research (A) “Multiferroics in Dirac electron materials” (No. 15H02108), Scientific Research (A) (No. 18H03880), Scientific Research (B) “Control of dynamics spin response in strong spin–orbit coupling systems” (No. 19H01850), and the Spintronics Research Network of Japan (Spin-RNJ), and then by the program of Research Fellowship for Young Scientists from the Japan Society for the Promotion of Science (JSPS), and also by Kyoto University Nano Technology Hub in “Nanotechnology Platform Project” sponsored by the MEXT, Japan.